









# Fluid evolution and hydrothermal alteration in the AN-34 and QT-02 IOCG prospects: clues for IOCG metallogenesis in the northern sector of the Carajás Mineral Province, Amazonian Craton

Gustavo Henrique Coelho de Melo<sup>1\*</sup> , Bruno Conty Serrão dos Santos<sup>2</sup> ,  
Roberto Perez Xavier<sup>3</sup> , Carolina Penteado Natividade Moreto<sup>2</sup> , Poliana Iara de Freitas Toledo<sup>4</sup> ,  
Gláucia Queiroga Nascimento<sup>1</sup> , Marco Paulo de Castro<sup>1</sup> , Fernando de Castro Paula<sup>5</sup> 

## Abstract

The AN-34 and QT-02 iron oxide–copper–gold (IOCG) prospects are located in the northern portion of Carajás Mineral Province (CMP), where important copper IOCG deposits occur. This region lacks basic geological information on the outskirts of the large IOCG deposits, and these small prospects might provide information regarding fluid–rock interaction and alteration–mineralization styles. In these prospects, banded iron formations (BIFs), basic volcanic rocks, and granitoids are variably deformed and hydrothermally altered. The hydrothermal alteration evolved from early silicification, potassic alteration, and Fe enrichment. All these alterations are pervasive and linked to shearing structure development. They are followed by late, ductile–brittle, chloritic alteration and sodic alteration. The quartz–magnetite oxygen isotope geothermometry ( $\delta^{18}\text{O}_{\text{qtz-mag}}$ ) and chlorite geothermometry reveal a decrease in the temperature of the hydrothermal system from  $520^\circ\text{C} \pm 30^\circ\text{C}$  to  $273^\circ\text{C} \pm 20^\circ\text{C}$ . The calculated  $\delta^{18}\text{O}_{\text{H}_2\text{O}}$  for silicification (6.6–5.8‰) and Fe enrichment (9.2–10.47‰) suggest the involvement of magmatic fluids.  $\delta^{18}\text{O}_{\text{H}_2\text{O}}$  values from 0.27 to 0.77‰ and 1.7 to 3.3‰ from late sodic alteration and hematite are compatible with meteoric fluids. Our findings shed more light on the fluid–rock interaction, hydrothermal evolution, and mineralization styles in the IOCG deposits of the northern sector of the CMP.

**KEYWORDS:** copper deposits; ore-forming processes; metallogenesis; stable isotopes.

## 1 INTRODUCTION

Iron oxide–copper–gold (IOCG) deposits have become important copper targets for mineral exploration and scientific research in the last three decades (Corriveau et al., 2016; Hitzman, 2000; Williams et al., 2005). In the last years, a set of new prospects including the Wirrda Well and Acropolis at Gawler Craton (Australia) and Nori and DeVries at Great

Bear Magmatic Zone (Canada) have been discovered and reported around world-class IOCG deposits. They are currently under economic evaluation aiming to increase copper reserves within these provinces (Kelly et al., 2020; Krneta et al., 2017). These prospects commonly have geological features that allow an understanding of giant deposits formed and evolved over space and time.

The Carajás Mineral Province (CMP) comprises one of the geochronological–tectonic provinces of the Amazonian Craton, north of Brazil. This province is world renowned for its remarkable metallogenetic potential and hosts a great variety of important ore deposits, including some of the most important IOCG deposits in the world, located in the Carajás Domain (CD), northern sector of the CMP (Xavier et al., 2012). This domain houses important copper-rich belts, i.e., the Northern Sector and Southern Copper Belt (Moreto et al., 2015a; Moreto et al., 2015b). The IOCG deposits are located within regional-scale E–W and WNW–ESE shear zones (e.g., Cinzento Shear Zone and Carajás Fault System, in the north and Canaã Shear Zone, in the south; Xavier et al., 2012).

At the northern sector of the CD, the complex tectono–magmatic–hydrothermal evolution of the deposits is observed in the styles and distribution of the hydrothermal alteration zones. This complexity can also be observed in

### Supplementary material

Supplementary data associated with this article can be found in the online version: [Supplementary Material](#).

<sup>1</sup>Universidade Federal de Ouro Preto, School of Mines, Department of Geology – Ouro Preto (MG), Brazil. E-mails: [gustavo.melo@ufop.edu.br](mailto:gustavo.melo@ufop.edu.br), [glauCIAqueiroga@ufop.edu.br](mailto:glauCIAqueiroga@ufop.edu.br), [marco.castro@ufop.edu.br](mailto:marco.castro@ufop.edu.br)

<sup>2</sup>Universidade Estadual de Campinas, Institute of Geosciences – Campinas (SP), Brazil. E-mails: [b.contyufopa@gmail.com](mailto:b.contyufopa@gmail.com), [cmoreto@unicamp.br](mailto:cmoreto@unicamp.br)

<sup>3</sup>Agência para o Desenvolvimento e Inovação do Setor Mineral Brasileiro – Brasília (DF), Brazil. E-mail: [roberto.xavier@adimb.org.br](mailto:roberto.xavier@adimb.org.br)

<sup>4</sup>Universidade Federal do Rio Grande do Norte, Department of Geology – Natal (RN), Brazil. E-mail: [toledopoliana@gmail.com](mailto:toledopoliana@gmail.com)

<sup>5</sup>Vale Company – Belo Horizonte (MG), Brazil. E-mail: [fernando.paula@vale.com](mailto:fernando.paula@vale.com)

\*Corresponding author.



the stable isotope studies and geochronological data, which reveals hybrid fluid sources and different episodes of copper mineralization (Hunger et al., 2018; Melo et al., 2017; Melo et al., 2019; Toledo et al., 2019).

Within this sector, the Cururu Region hosts the AN-34 and QT-02 prospects, close to important IOCG deposits (e.g., Salobo, Furnas, and GT-46). These targets exhibit a particular geological scenario, where the hydrothermal processes occur over the host rocks, and changes in mineralogy, texture, and color can be clearly seen. Banded iron formation (BIF), basic volcanic rocks, and granitoids are variably deformed and hydrothermally altered. These rocks grade from unaltered rocks to strongly hydrothermally altered ones with grunerite–almandine–magnetite-rich rocks and chlorite-rich rocks, but the primary features of the host rocks (i.e., mineralogy and textures of the hosts) are still recognized.

These findings contrast with the giant Salobo and Furnas, where relicts of the hosts are scarce or absent and do not provide much regional geological information about the country rocks (Jesus, 2016; Melo et al., 2017). These changes in the hosts and the hydrothermal mineral paragenesis reveal important information on fluid–rock interaction in the northern sector of the CD. In addition, the different styles of mineralization observed within these prospects could reflect distinct periods of ore formation in the northern sector for the CD.

In this study, we investigate the metallogenetic evolution of the AN-34 and QT-02 prospects by identifying host rocks, examining fluid–rock interaction, and characterizing the evolution of hydrothermal alteration halos and distinct mineralization styles. We employ chlorite chemistry and oxygen-stable isotope analysis to elucidate the sources and evolution of the ore-forming fluids. The metallogenetic processes observed both within and adjacent to these prospects enhance our understanding of regional-scale ore-forming mechanisms that could guide future prospecting surveys in the area, particularly for IOCG deposits.

## 2 CARAJÁS MINERAL PROVINCE GEOLOGICAL SETTING

The CMP represents the only Archean nucleus (Santos et al., 2000; Santos, 2003) in the Amazonian Craton (Fig. 1A). The CP is divided into two tectonic domains: Rio Maria Domain (RMD) in the south and CD in the north, revealed by trans-lithospheric structures as a result of the collision between these two terrains (Martins et al., 2017; Vasquez et al., 2008; Figs. 1B and 1C).

The Mesoproterozoic (ca. 3.0–2.83) basement rocks of the CD include gneisses, migmatites, granulites, a diversity of granitoids, and fragments of greenstone belt sequences (Vasquez et al., 2008, and references therein).

Basement rocks are overlain by a set of Neoproterozoic volcano-sedimentary sequences. These sequences are mainly represented by Aquiri, Liberdade, São Félix Groups, and Itacaiúnas Supergroup (ca. 2.76–2.73 Ga, Costa et al., 2016, DOCEGEO, 1988). The Itacaiúnas Supergroup is the most ubiquitous supracrustal in the central and northern parts

of the CD. This supergroup is divided into lower mafic volcanic rocks, intermediate chemical sedimentary rocks, and upper siliciclastic sedimentary rocks (Tavares et al., 2018). Likewise, this supergroup can be divided into Serra da Bocaina and Grão Pará groups (Costa et al., 2016). Within the Serra da Bocaina Group, the Salobo-Pojuca Formation, with BIFs and basic volcanic and siliciclastic sedimentary rocks (Costa et al., 2016), hosts most of the IOCG deposits in the northern sector of the CD.

Mafic-ultramafic layered bodies include the Luanga Complex, Vermelho, mafic rocks of the Santa Inês gabbro, and the Pium diopside norite (Vasquez et al., 2008). Three granitic magmatism events occurred in the CD. The first, from 2.76 to 2.73 Ga, generated syntectonic, foliated, alkaline, and metaluminous granites (e.g., Barbosa, 2004; Barros et al., 2009; Estrela, Planalto, and Igarapé Gelado suites; Feio et al., 2012). At ca. 2.57 Ga, there were several occurrences of peralkaline to metaluminous granitoids (e.g., Old Salobo and Buritirama granites, Machado et al., 1991; Salgado et al., 2019). The existence of this granite magmatism, however, has been debatable in recent works (e.g., Toledo et al., 2023). In ca. 1.88 Ga, A-type anorogenic, alkaline to subalkaline, and metaluminous to slightly peraluminous granites (e.g., Central de Carajás and Cigano) are widespread (Machado et al., 1991). Paleoproterozoic siliciclastic units partially cover the Itacaiúnas Supergroup and consist of Águas Claras and Buritirama formations (Araújo Filho et al., 2020).

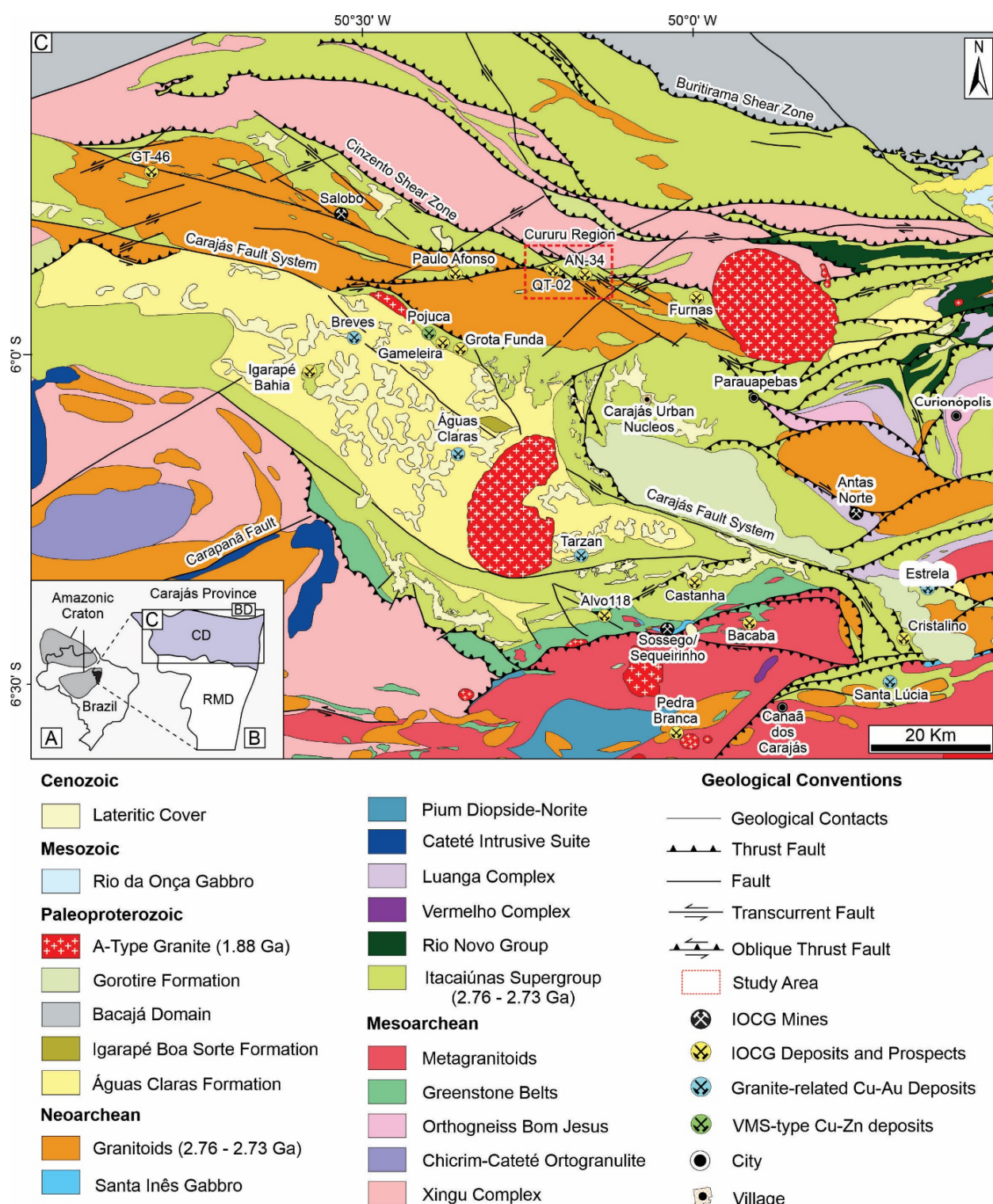
This complex evolution of the CMP gave origin to a set of IOCG deposits during the Neoproterozoic (2.71–2.68 Ga and ca. 2.55 Ga) and Paleoproterozoic (1.88 Ga; Moreto et al., 2015b, Trunfull et al., 2020). The deposits formed in the Neoproterozoic commonly exhibit higher temperatures associated with ductile deformation due to shearing, whereas those formed in the Paleoproterozoic display lower-temperature conditions associated with brittle deformation (Moreto et al., 2015a; Moreto et al., 2015b). They can also be divided into the deposits located in the Southern Sector (or Southern Copper Belt; e.g., Sossego, Alvo 118, and Cristalino), along the Canaã Shear Zone, and those at the Northern Sector (e.g., Salobo, Igarapé Bahia, and Furnas; Xavier et al., 2012), along the Cinzento Shear Zone.

## 3 METHODS

This research has been primarily developed over drill cores and local fieldwork in the AN-34 and QT-02 prospects. Petrographic studies and scanning electron microscopy (SEM) provided more detailed geological information for the deposits. The following methods included mainly mineral chemistry and stable isotope analyses.

### 3.1 Drill core logging, petrography, and scanning electron microscopy

A detailed description of two drill cores from the AN-34 (FD0003 and FD0005) and three from the QT-02 (FD004, DH007, and DH018) prospects was made during fieldwork. Polished thin sections were analyzed under transmitted and reflected light under an optical microscope.



IOCG: iron oxide–copper–gold; VMS: volcanogenic massive sulfide.

Source: modified from Costa et al. (2016).

**Figure 1.** (A) Location of the Carajás Mineral Province (CMP) within the Amazon Craton, Brazil. (B) Compartmentation of the CP into Rio Maria Domain (RMD) in the south and the Carajás Domain (CD) in the north. (C) Simplified geological map of the CD with the location of the main ore deposits and regional structures. Red boxes show the location of AN-34 and QT-02 prospects.

Complementary investigations on metalized thin sections with a carbon coating using a Zeiss LEO 430i SEM coupled with energy-dispersive X-ray spectrometer (EDS) were carried out at the SEM Laboratory of the Geosciences Institute of Universidade Estadual de Campinas (UNICAMP), Brazil. This method was only used as a semi-quantitative analysis to reveal the occurrence of minor mineral phases.

### 3.2 Mineral chemistry

Chlorite mineral chemistry was performed in two representative thin sections from the QT-02 and AN-34 prospects. Electron microprobe analysis (EMPA) was performed using a JEOL JXA-8230 microprobe, equipped with five wavelength-dispersive spectrometers (WDS) and with one EDS, in cooperation with the Microscopy and Microanalysis Laboratory (LMic) of



the Universidade Federal de Ouro Preto (UFOP). The operating conditions were 15 kV accelerating voltage, 20 mA beam current, and 2  $\mu$ m beam diameter. The elements analyzed are followed by the used natural standards (in parentheses): Na (anorthoclase), F (calcium fluoride), Si (quartz), Al (anorthite), Mg (olivine), Zn (gahnite), Fe (magnetite), Cl (scapolite), Cr (chromite), Ni (Ni), P and Ca (fluor-apatite), Mn (Mn), Ti (rutile), and K (microcline). The total iron content was taken as FeO.

From a total of 83 microprobe analyses of chlorite, 16 were excluded due to their anomalous Si weight percent (wt%). The *WinCcac* software (Yavuz et al., 2015) was used to calculate the chlorite cationic distribution, based on 18 cation formulae (i.e.,  $O_{10}(OH)_8 = 14$  equivalent oxygen), according to Association Internationale Pour l'Étude des Argiles [AIPEA], Guggenheim et al., 2006). This software estimates  $H_2O$  (wt%),  $Fe_2O_3$  (wt%), and FeO (wt%) amounts of chlorite analyses obtained from electron microprobe  $FeO_{tot}$  (wt%). Temperatures of chloritization were calculated based on empirical equations proposed by several authors using the same software. The graphics were made using the software Grapher 14, from Golden Software. The analytical results are included in the Supplementary Data.

### 3.3 Oxygen-stable isotope analyses

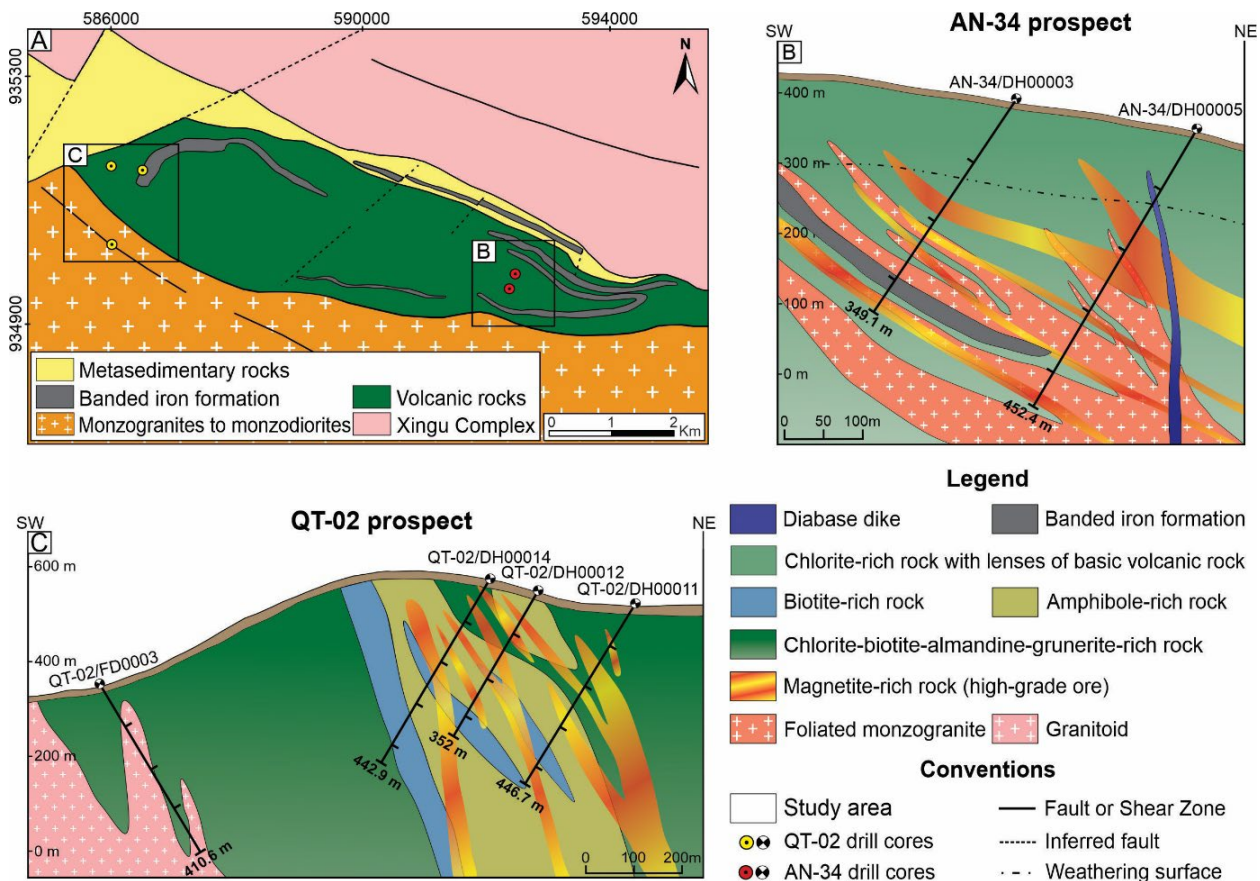
Oxygen-stable isotope analyses ( $\delta^{18}O$ ) were performed on different quartz, magnetite, hematite, and albite generations of the AN-34 and QT-02 prospects. Minerals were extracted from drill core samples, crushed into an agate mortar, and then

taken to mineral separation under a binocular loupe (hand picking), separating approximately 2–5 mg of pure mineral concentrates. Oxygen isotopes were measured using a laser fluorination procedure, which involved the sample reaction with excess  $ClF_3$  using a  $CO_2$  laser at temperatures around 1,500°C (Sharp, 1990). Oxygen isotopic composition was determined on cryogenically cleaned  $CO_2$  at a VG SIRA II spectrometer at the Scottish Universities Environmental Research Center, University of Glasgow, Scotland. The values of  $\delta^{18}O$  were expressed in permil delta notation ( $\delta, \text{‰}$ ), relative to the Vienna Standard Mean Ocean Water (VSMOW).

## 4 GEOLOGY OF THE AN-34 AND QT-02 IOCG PROSPECTS

The AN-34 and QT-02 copper prospects are located in the Cururu Region, in the north most part of the WNW-ESE Cinzento Shear Zone (Figs. 1 and 2A). In this region, volcano-sedimentary rocks from the Salobo-Pojuca Formation, Itacaiúnas Supergroup, and granitoids from the Igarapé Gelado suite are the main hosts of the mineralization (Fig. 2). In the prospects' area, the sequence consists of BIFs and basic volcanic rocks. In addition, foliated to isotropic monzo- to syenogranite also hosts copper mineralization (Figs. 2B and 2C).

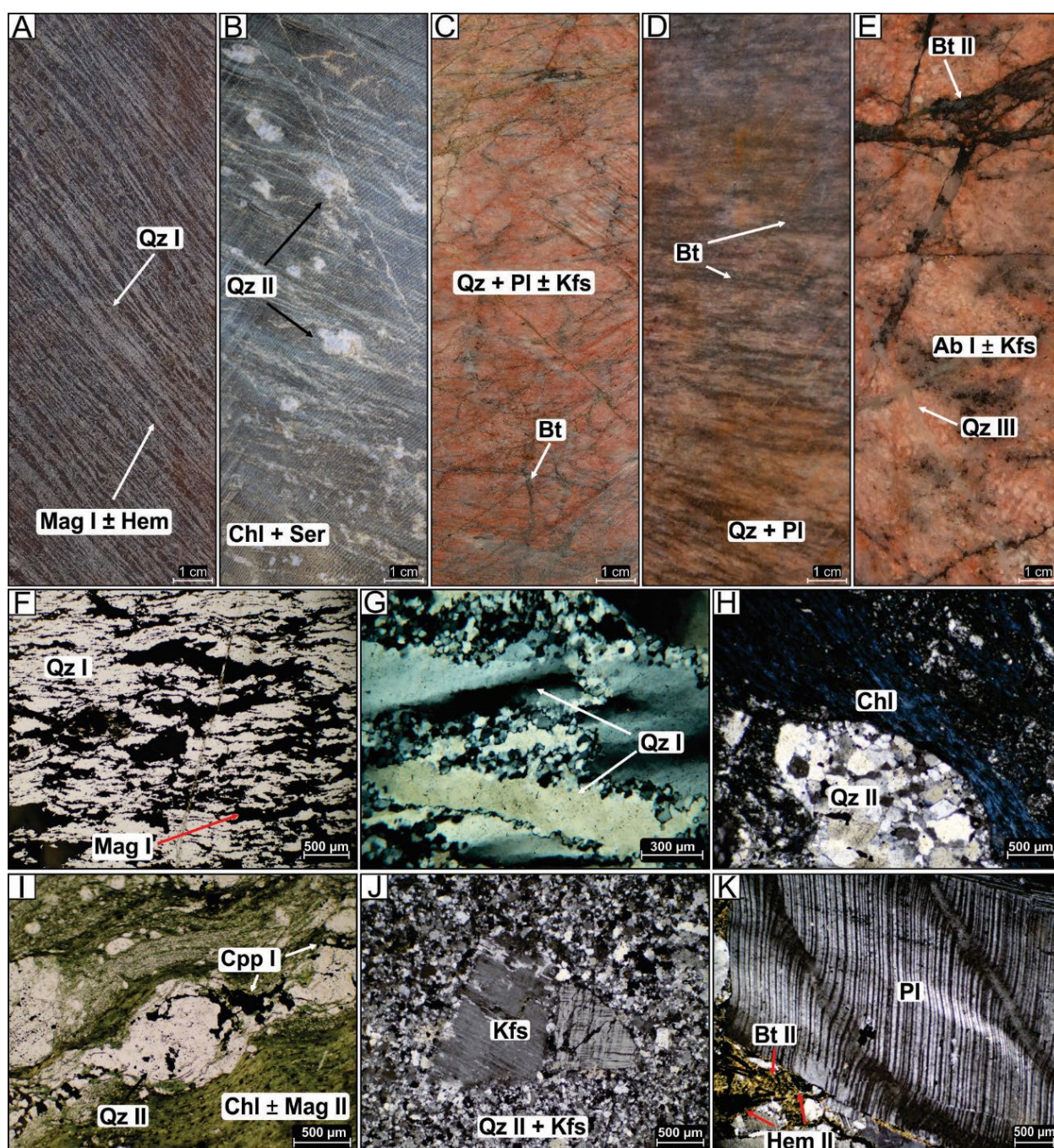
The original features of the main host rocks were partially obliterated by hydrothermal alteration and deformation due to shearing (Figure 3). Intense hydrothermal alteration over the



Source: modified from Vale (2018).

**Figure 2.** (A) Geological map of the Cururu Region displaying the AN-34 and QT-02 prospects. (B) Cross-sections of the AN-34 and (C) QT-02 prospects showing the spatial distribution of host rocks, hydrothermally altered rocks, and mineralized zones.





Ab: albite; Bt: biotite; Chl: chlorite; Ccp: chalcopryite; Hem: hematite; Kfs: potassium feldspar; Mag: magnetite; Pl: plagioclase; Qz: quartz; Ser: sericite.

**Figure 3.** Main aspects of the AN-34 and QT-02 prospects' lithotypes. (A to E) Drill core samples. (F) Transmitted light/plane-polarized light and (G to K) transmitted light/cross-polarized light photomicrographs. (A) The BIF consists of alternating layers of quartz I and magnetite I. (B) Deformed basic volcanic rock showing amygdaloidal texture filled with quartz II. (C) Isotropic and (D) foliated portions of monzogranite at the AN-34 prospect. (E) Weakly altered granitoids from the QT-02 prospect cut by quartz III and biotite III veinlets. (F) Recrystallized quartz I and elongated magnetite I parallel to primary compositional banding. (G) Quartz I ribbon with recrystallized envelope. (H) Amygdale filled with quartz II surrounded by a mixture of chlorite I, quartz II, and sericite. (I) Quartz I sigmoid contoured with chalcopryite inclusions immersed in chlorite I+magnetite II+sericite-rich matrix. (J) Potassium feldspar phenocryst surrounded by subgrains of quartz and potassium feldspar. (K) Coarse-grained plagioclase with bent twinning associated with biotite II- and hematite-rich zones.

hosts gave origin to extremely altered and sheared lithotypes, such as grunerite–almandine–magnetite-rich and chlorite-rich rocks, which envelop the copper ore zones.

#### 4.1 Banded iron formations

BIFs can be found in both prospects. At the AN-34, BIFs display discontinuous bands of variable thickness interleaved with chlorite-rich rocks. On the contrary, in the QT-02, a thick

pack of preserved BIFs interlayered with lenses of basic volcanic rocks is broadly recognized.

In the most preserved zones, the BIFs are fine- to medium-grained, with layers ranging from 0.5 to 2.5 cm in thickness, and the compositional layering is typically marked by the alteration of quartz (50%) and magnetite (40%) (Figs. 3A), with small amounts (5%) of other minerals, including hematite and carbonates. Locally, the BIFs exhibit folds, fractures,



breccias, and stockwork zones. The quartz is fine-grained (< 1.2 mm) with undulose extinction. In some portions of the BIF, granoblastic texture and quartz ribbons can be observed (Fig. 3G). Magnetite is fine-grained (< 0.5 mm), is xenomorphic, and is commonly replaced by hematite. Recrystallized quartz and stretched magnetite parallel to primary compositional banding define the mylonitic foliation (Figs. 3F and 3G).

With the increase of the hydrothermal alteration and deformation features (i.e., shearing), this lithotype grades into rocks with hydrothermal minerals, such as almandine, grunerite, and chlorite. In these zones, an anastomosed foliation overprints primary bedding.

## 4.2 Basic volcanic rocks

The basic volcanic rock occurs as small wedges within the AN-34, but its recognition is tricky, and primary textures are poorly preserved. This rock commonly appears hydrothermally altered with a greenish color and fine- to medium-grained and mylonitized texture. It contains very fine-grained lamellar chlorite I and sericitic foliated groundmass. Amygdales of up to 1 cm are filled with fine-grained quartz I and chlorite I and, locally, have pressure shadows (Figs. 3B and 3H). Primary igneous minerals are completely replaced by hydrothermal minerals (i.e., chlorite).

Particularly at AN-34, this rock grades to zones where a greenish-gray color and fine- to medium-grained texture predominate with mylonitic foliation. These zones contain fine- to medium-grained xenomorphic quartz I with undulose extinction and lobate contact with minerals that comprise the matrix. The matrix is composed of fine-grained magnetite I, sericite, and chlorite I with minor tourmaline and biotite I. These minerals define the mylonitic foliation and can be locally observed in quartz sigmoids with minor chalcopyrite I inclusions (Fig. 3I).

## 4.3 Granitoids

At AN-34, granitoids are reddish to gray, phaneritic, equigranular, and fine- to medium-grained (< 5 mm). Foliated portions with shear bands can often be observed (Fig. 3C), although some portions are isotropic (Fig. 3D). They are primarily monzogranites composed of magmatic quartz (35%), plagioclase (30%), orthoclase (25%), biotite, epidote, and allanite (5%). Carbonate and sericite (5%) are also recognized. Hydrothermal chlorite I and stretched quartz I can be observed in altered zones and define the foliation.

Quartz grains are fine- to medium-grained (< 2 mm), are xenomorphic, and show interlobate boundaries with plagioclase and potassium feldspar. Also, quartz crystals in the granitoids show undulose extinction, subgrain formation, and well-defined grain orientation. Plagioclase and potassium feldspar are fine- to medium-grained (< 1.5 mm), mostly xenomorphic with idiomorphic grains in less-deformed portions. Locally, potassium feldspar phenocrysts can also be observed surrounded by fine-grained recrystallized potassium feldspar and quartz (Fig. 3J), often with kink bands.

Granitoids at QT-02 display a stronger hydrothermal alteration; nevertheless, some weakly altered portions can be observed (Fig. 3E). These pink phaneritic rocks are medium- to coarse-grained (< 4 mm). Primary mineralogy is partially replaced by hydrothermal minerals.

## 5 HYDROTHERMAL ALTERATION

The styles and paragenetic evolution of the hydrothermal alteration at AN-34 and QT-02 are quite similar (Figs. 4A and 4B). However, the reconstruction of the temporal evolution of the hydrothermal system was individually described here based on the different stages of alteration and deformation structures (Figs. 5A–5C).

The early stages of hydrothermal alteration are represented by (i) silicification, (ii) Fe enrichment (grunerite, magnetite I, and almandine), and (iii) potassic alteration with biotite zones, which enclose the copper mineralization. A second stage of (iv) silicification is accompanied by the second stage of mineralization. Intense (v) chloritic alteration overlaps previous alterations. A (vi) second stage of potassic alteration with biotite is better developed at the QT-02 prospect. These alterations and the associated mineralization are related to the development of ductile structures (i.e., shearing), including shear bands and penetrative mylonitic foliation. Whereas chloritic alteration can reach around 500 m away from the central zone of the prospects; the other hydrothermal alterations are narrower and have inner halos, with an envelope of 100–200 m around copper mineralization (Figs. 2A and 2B). Fe enrichment is often developed over the BIF and in its borders. Crosscutting relationships and telescoping are commonly observed when younger hydrothermal alterations overprint older ones.

The late stage of hydrothermalism includes sodic alteration zones with (vii) albite, which is mainly observed in the QT-02 prospect. In these zones, hydrothermal biotite, hematite, and chalcopyrite can be observed. Late (viii) veins and veinlets (carbonate–chlorite–quartz–albite–chalcopyrite) are also found. These late hydrothermal alterations affected the inner zones of the deposit and crosscut the earlier hydrothermal alteration.

### 5.1 Silicification I

Silicification I is widespread in both prospects, in fronts of replacement and veins. In basic volcanic rocks, silicification I is pervasive, where quartz I constitutes the rock matrix (Figs. 6A and 7A). In BIFs at the QT-02 prospect, quartz I grows along the foliation and forms stretched bands. The quartz of silicification I is fine- to medium-grained, is subidiomorphic to xenomorphic, and concordant with the foliation. Undulose extinction, subgrain formation, sigmoids, bands, and ribbons are frequent in this generation of quartz.

### 5.2 Fe enrichment

The Fe enrichment zones appear as fronts and pockets within the prospects. It encompasses early magnetite I  $\pm$  quartz I followed by grunerite+almandine  $\pm$  chlorite I, and it is best



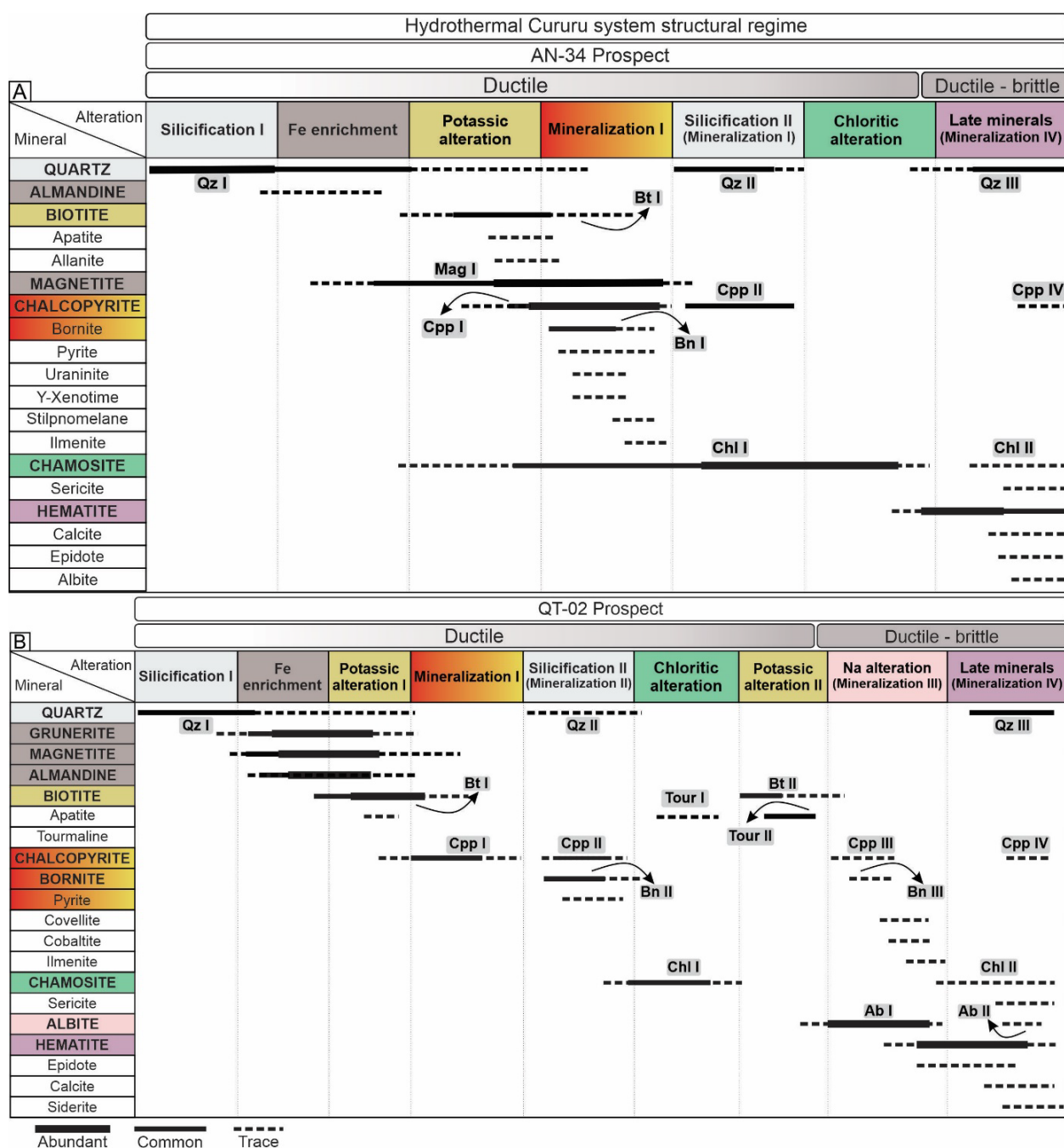


**Figure 4.** Paragenetic sequence of the AN-34 and QT-02 prospects, divided into (A) AN-34 and (B) QT-02 prospects showing the mineral alteration sequence and mineralization stages.

seen at QT-02. In QT-02, the most preserved BIF and lenses of basic volcanic rock grade to hydrothermally altered zones with grunerite, almandine, and magnetite. At AN-34, relicts of this alteration can also be present but strongly altered to chlorite formation.

In the QT-02 prospect, magnetite I is fine-grained, often subidiomorphic to idiomorphic, associated with quartz I + grunerite crystals (Fig. 6B). The central domain of the AN-34 is marked by intense Fe enrichment depicted by large amounts of massive magnetite I ± quartz I. In these zones, magnetite-rich lenses define the mylonitic foliation (Fig. 6C) associated with chalcopyrite (mineralization I; Fig. 8B).

Grunerite is oriented along quartz I- and magnetite I-rich microbands (Figs. 6B and 7C). This is accompanied by a

gradual growth of almandine + magnetite I ± chlorite I (Fig. 6D). Almandine is essentially idiomorphic and rounded, consisting of fine- to coarse-grained (< 1 mm–1.2 cm, Fig. 7D).

### 5.3 Potassic alteration

Potassic alteration with biotite I is restricted in both prospects, particularly over the granitoids. It is represented by biotite I ± quartz I ± magnetite, defining planes of mylonitic foliation. This is commonly replaced by pervasive chlorite I (Fig. 7E). At AN-34, though partially replaced by later chlorite, biotite is better developed close to mineralized zones. Biotite I is fine-grained, is subidiomorphic to xenomorphic, and forms platy crystals up to 1 mm, associated with quartz I ribbons.

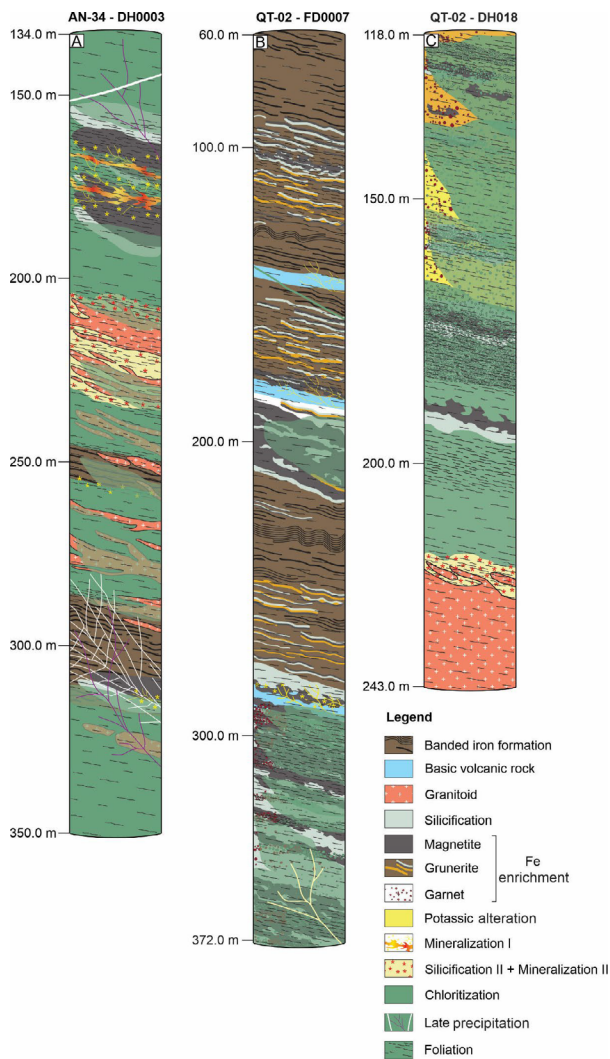


**Figure 5.** Schematic stratigraphic sequence of the (A) AN-34 and (B and C) QT-02 prospects based on four representative drill cores, showing hydrothermal altered zones and copper mineralization.

## 5.4 Main copper mineralization

At least four stages of copper mineralization have been identified in the prospects with different styles and structural controls. The main stage of mineralization in terms of economic importance (i.e., grades) is represented by mineralization I. It forms elongated lenses concordant to the mylonitic foliation. Zones of intense Fe enrichment and potassic alteration with biotite I are the locus of the copper ore.

Mineralization I is more abundant in the AN-34 prospect but also appears at QT-02. It consists chiefly of disseminated to massive chalcopyrite I (45%) strongly associated with magnetite (40%) and minor bornite I (5%) and pyrite I (5%) (Figs. 8A and 8B). Chalcopyrite veinlets are also recognized. Uraninite, Y-xenotime, allanite, apatite, and ilmenite are common accessory minerals within the ore zones and encompass 5% of the ore. They appear as inclusions within chalcopyrite I and magnetite I.

Chalcopyrite I is fine- to medium-grained (< 4 mm), is xenomorphic, is granular to massive, and is mainly associated with magnetite I crystals (Figs. 8F and 8G). Stilpnomelane appears as acicular crystals included within chalcopyrite I (Fig. 8H). Bornite I is fine-grained, xenomorphic, and granular.

Minor pyrite I usually forms xenomorphic crystals associated with quartz I and chalcopyrite I (Fig. 8I).

## 5.5 Silicification II + mineralization II

The silicification II with quartz II is an incipient alteration, mainly developed and associated with the granitoid observed at the AN-34 prospect (Figs. 5A, 5C, and 6E). Quartz II occurs as medium-grained, idiomorphic to subidiomorphic with undulose extinction and ribbons. The mineralization II is poorly developed and is comprised of chalcopyrite II (85–95%) and bornite II (5%) within quartz II. In these zones, chalcopyrite II and bornite are granular, are fine-grained, and fill the spaces between quartz II crystals (Fig. 8C). This mineralization is mainly observed near the granitic apophysis (Fig. 8D) and subordinately can also occur in massive zones. Generally, dendritic covellite replaces bornite II (Fig. 8K) where cobaltite can also be recognized.

## 5.6 Chloritic alteration

Chloritic alteration is the most important and extensive type of hydrothermal alteration in both prospects and surrounding areas. It is pervasive and mainly associated with mylonitic zone development (Figs. 6F, 6G, 6H, and 6L) and forms a proximal halo around the ore zones. It reveals fine-grained (< 1 mm) lamellar, Fe-rich chlorite (i.e., chamosite) and minor sericite ± epidote. Most of the previous alterations and host rocks were overprinted by chlorite I formation. In mylonitized zones, chlorite occurs as strongly selective alteration fronts. In these zones, grunerite and biotite I are converted into chamosite (Fig. 7E). At completely chloritized domains, chlorite pseudomorphs after garnet are frequently observed (Figs. 6G and 7G).

## 5.7 Potassic alteration II

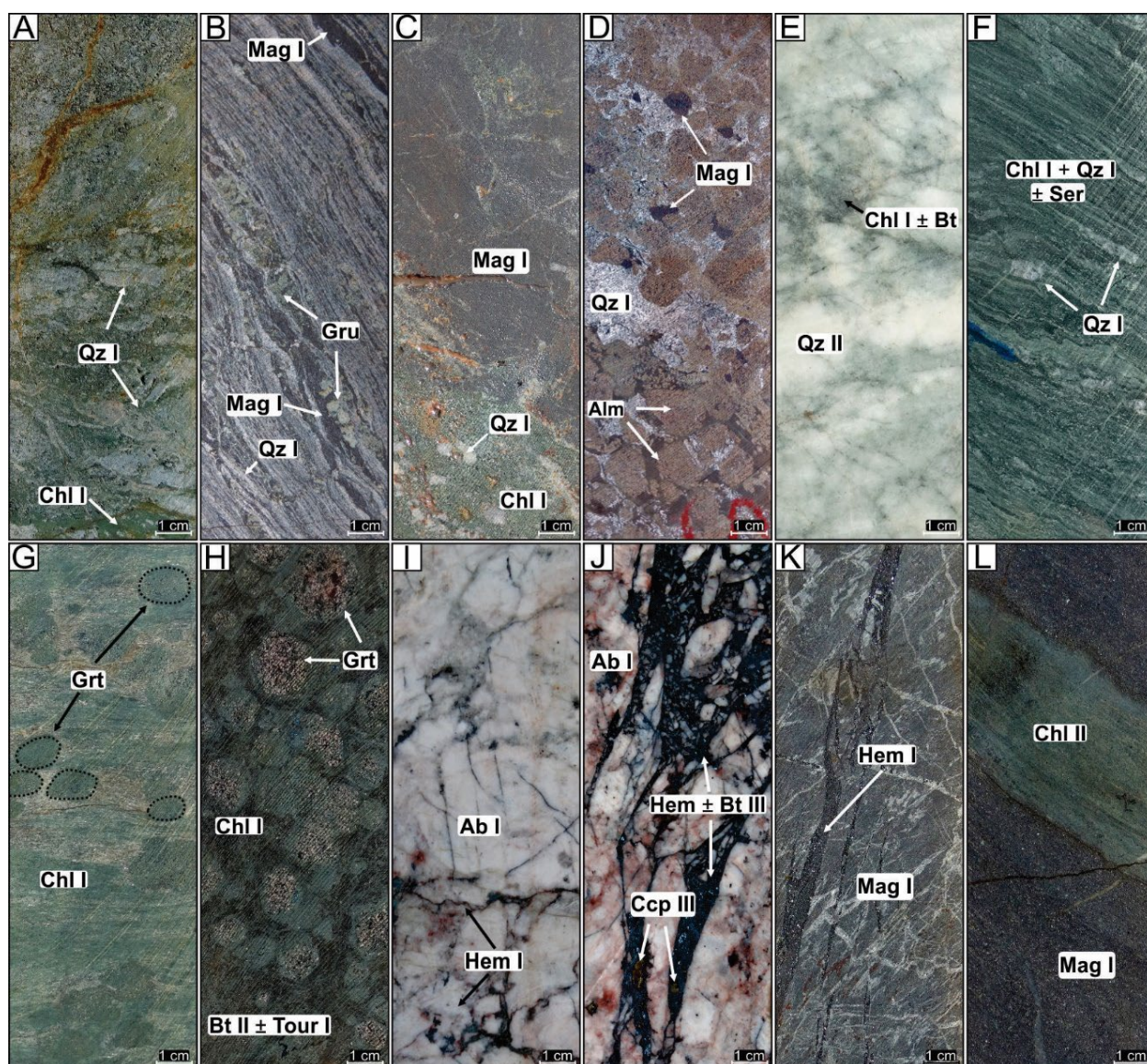
A second stage of potassic alteration with biotite can be observed at the QT-02 prospect. It is represented by biotite II ± tourmaline I ± apatite ± (quartz II) and overlaps part of the Fe enrichment assemblage (i.e., grunerite). The biotite II forms coarse lamellar crystals (0.5–1.4 mm) and defines the mylonitic foliation. Furthermore, the biotite II surrounding almandine crystals was replaced entirely or partially by chlorite I (Figs. 6H and 7H).

Grunerite is commonly replaced by biotite II (Fig. 7F). Subordinate amounts of quartz II, tourmaline I aggregates, and apatite accompany the potassic alteration. Tourmaline I crystals are medium- to coarse-grained (up to 4 mm long), idiomorphic, and zoned (Fig. 7I). In sheared zones, tourmaline I crystals are fine-grained and stretched along the mylonitic foliation.

## 5.8 Sodic alteration

The sodic alteration is recognized mainly in the QT-02 and in some portions of the AN-34. This is mainly developed over the granitoids through the replacement of igneous feldspar where tiny hematite inclusions occur within the hydrothermal albite (Fig. 6I). This alteration marks the transition of ductile to ductile-brittle deformation. These crystals differ





Ab: albite; Alm: almandine; Bt: biotite; Chl: chlorite; Ccp: chalcopryrite; Gru: grunerite; Hem: hematite; Mag: magnetite; Qz: quartz; Ser: sericite; Tur: tourmaline.

**Figure 6.** Drill core photographs of hydrothermally altered rocks at AN-34 and QT-02. (A) Pervasive silicification I in basic volcanic rocks. (B) Quartz I+magnetite I+grunerite formation parallel to the mylonitic foliation in the banded iron formation. (C) Strongly chloritized rock with magnetite I fronts concordant with foliation. (D) Fe enrichment with the formation of almandine, magnetite I, and quartz I. (E) Intensively silicified II domain. (F) Chlorite-rich mylonitic rock showing mainly stretched quartz I. (G) Garnet xenoblastic crystals and grunerite replaced by chlorite I. (H) Biotite II+Tour I-rich zone with almandine crystals totally or partially replaced by chlorite I. (I) Granite affected by pervasive Na alteration with hematite I inclusions. (J) Hydrothermal breccias with hematite I-rich matrix in granite affected by Na alteration. (K) Stockwork zone in BIFs cut by late hematite veinlets. (L) Late chlorite II vein cutting massive magnetite I zone.

from preserved igneous feldspar crystals for showing chess-board twinning (Fig. 7J), undulose extinction, and bulging recrystallization that cut the primary feldspar.

### 5.9 Late veins, breccias, and mineralization

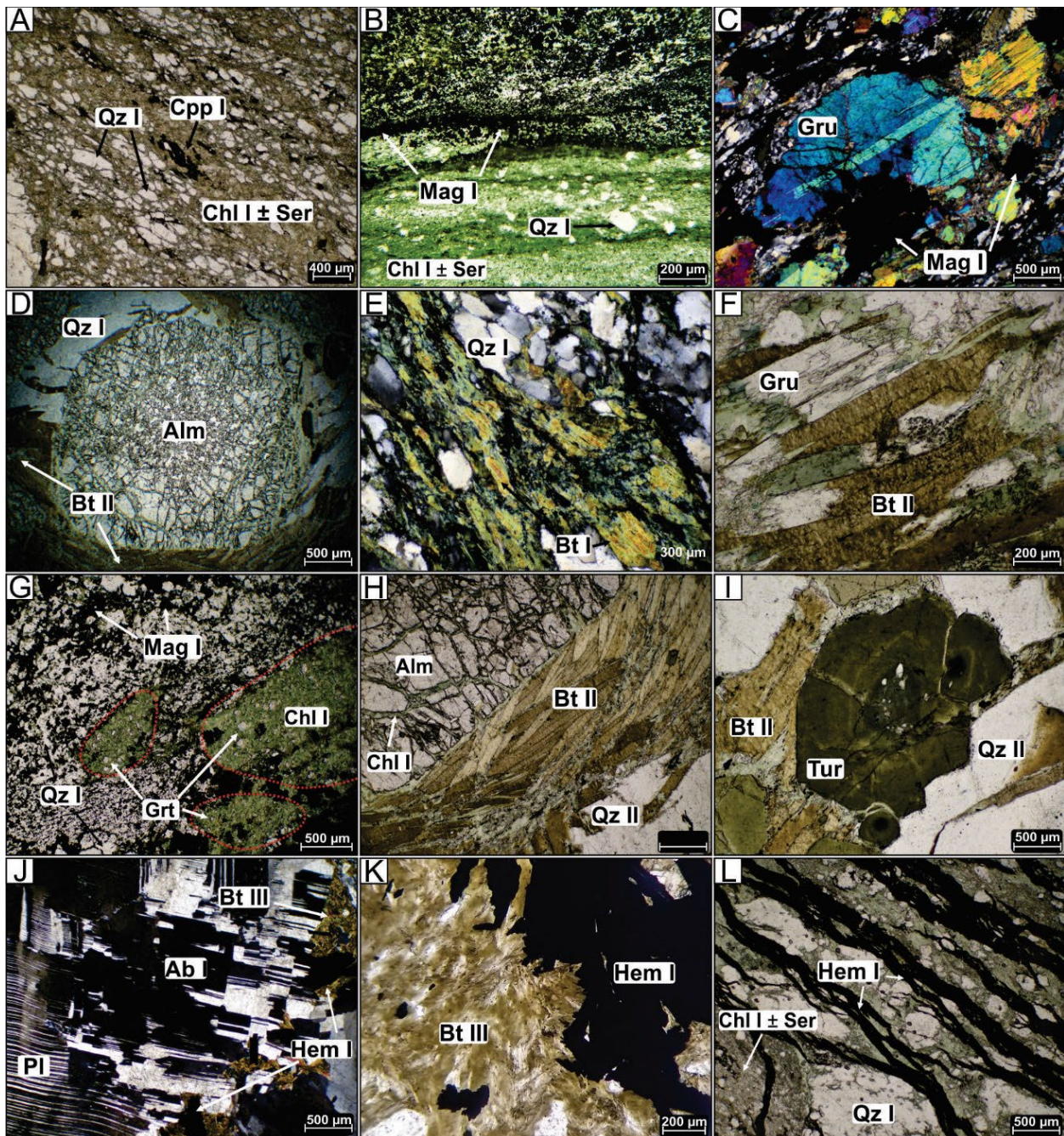
A diversity of late veins, veinlets, stockwork zones, and hydrothermal breccias are observed at the AN-34 and QT-02 prospects and mark the latest stage of hydrothermal activity in the region. Late copper mineralization (mineralization III and IV) is associated with brittle deformation.

Massive breccias comprised of magnetite I and quartz II are recognized within hydrothermally altered zones at basic volcanic rocks and BIFs. In the granitoids, angular clasts of albite

II are surrounded by a matrix of fine- to medium-grained (< 1 mm) specular hematite I crystals and fine (< 0.5 mm) brownish lamellar biotite III (Figs. 6J and 7K). Occasionally, amounts of granular and disseminated bornite III and chalcopryrite III are also found dispersed in the hematite I–biotite III-rich breccia (Fig. 8M), which comprises mineralization III (Figs. 8L–8N). This breccia evolves to zones where veins larger than 2 cm of hematite I are observed in both prospects (Figs. 6K and 7L).

A set of late veins and veinlets are filled with carbonate, chlorite II (Fig. 6L), albite II, biotite III, quartz III, epidote II, and chalcopryrite IV (i.e., mineralization IV). At QT-02, veins and veinlets of chlorite II and carbonate are more frequent. At AN-34, veins and veinlets of calcite, epidote II, and biotite III and milky quartz veins containing tourmaline II aggregates are predominant.





Ab: albite; Alm: almandine; Bt: biotite; Chl: chlorite; Ccp: chalcopryrite; Grt: garnet; Gru: grunerite; Hem: hematite; Mag: magnetite; Pl: plagioclase; Qtz: quartz; Ser: sericite; Tur: tourmaline.

**Figure 7.** Photomicrographs showing distinct stages of hydrothermal alteration in both prospects. (A) Strongly deformed idioblastic to subidioblastic quartz I, concordant to mylonitic foliation. (B) Xenoblastic magnetite I stretched and associated with chlorite I. (C) Twinned coarse-grained grunerite crystal displaying foliation in BIFs. (D) Fractured almandine poikiloblastic involved by biotite II. (E) Biotite II replaced by chlorite in quartz I mylonitic zones. (F) Biotite II replacing chloritized grunerite. (G) Garnet pseudomorphosed by chlorite II associated with magnetite I and quartz I. (H) Potassic alteration with biotite II surrounding idioblastic almandine partially chloritized. (I) Zoned tourmaline associated with biotite II and minor quartz II. (J) Hydrothermal albite showing chessboard texture. (K) Specular hematite I and biotite III in hydrothermal breccias at QT-02 granite affected by Na alteration. (L) Hematite I veinlets concordant to mylonite foliation in quartz I-rich zone. (A, B, D to I, K, and L) Plane-polarized light and (C and J) cross-polarized light.

## 6 CHLORITE GEOTHERMOMETRY

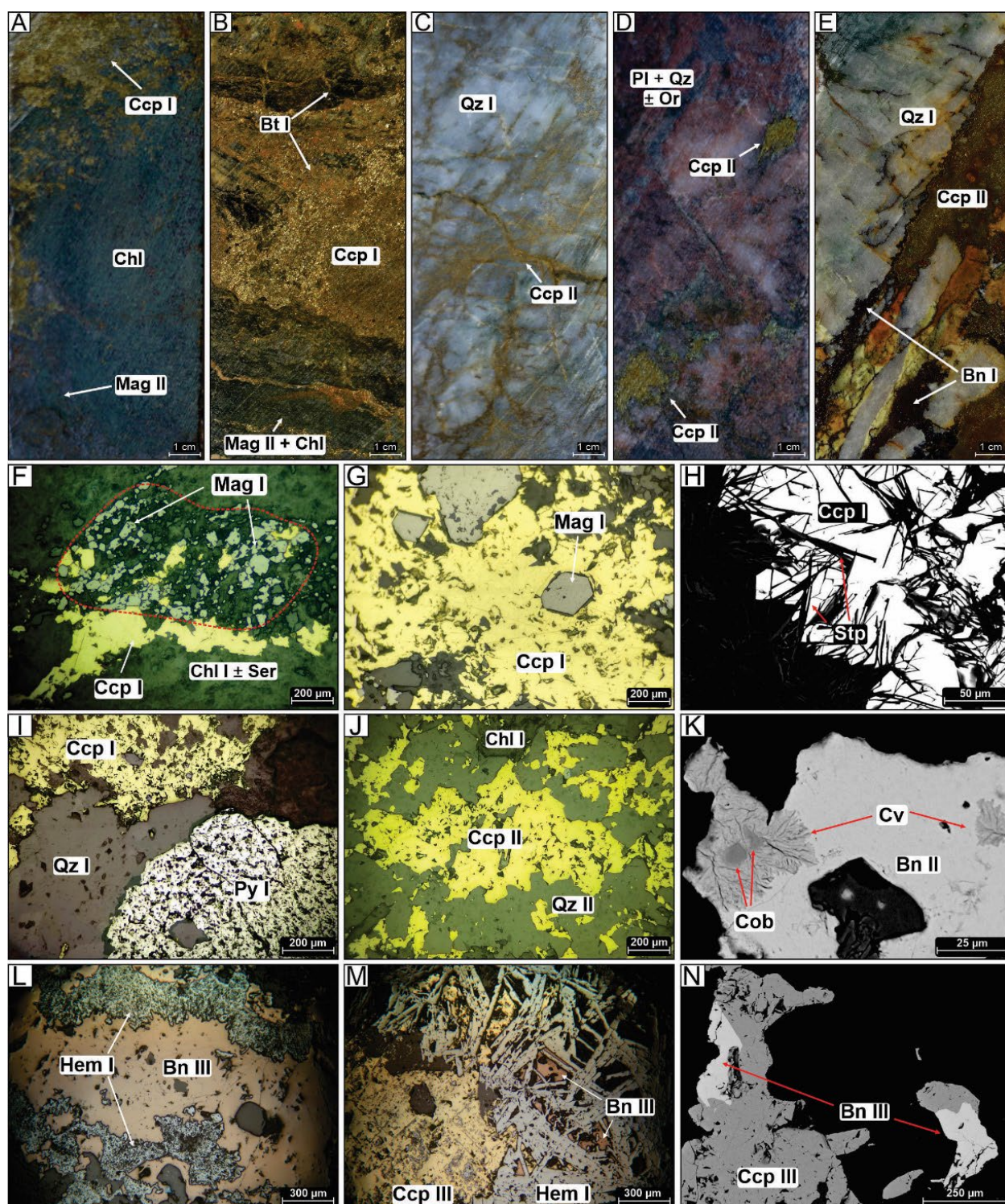
Mineral chemistry analyses of chlorite associated with mineralization I (i.e., chlorite I) from AN-34 and in late veins in BIFs (chlorite II) from QT-02 prospects were obtained and are shown in Table 1. The classification of chlorite was based on AIPEA (Guggenheim et al., 2006).

Chlorite from AN-34 and QT-02 does not display significant variations in terms of Fe and Al contents, classified

as chamosite ( $(\text{Fe}^{2+}, \text{Mg}, \text{and } \text{Fe}^{3+})_5\text{Al}(\text{Si}_3\text{Al})\text{O}_{10}(\text{OH}, \text{O})_8$ ) (Figs. 9A and 9B). In addition, there is no important variation in  $\text{Fe}/(\text{Fe}+\text{Mg})$  ratios, from 0.58 to 0.64 in chlorite I from AN-34 and 0.54 to 0.63 in chlorite II at QT-02, showing a slight negative correlation.

The  $\text{Al}^{\text{IV}}$  contents in chlorite I display a moderate-to-positive correlation with  $\text{Fe}/(\text{Fe}+\text{Mg})$  ratios, from 1.10 to 1.38 (Fig. 9C). Conversely, chlorite II presents a negative correlation, varying





Bn: bornite; Bt: biotite; Chl: chlorite; Ccp: chalcopyrite; Mag: magnetite; Or: orthoclase; Pl: plagioclase; Qz: quartz; Cob: cobaltite; Cv: covellite; Hem: hematite; Stp: stilpnomelane.

**Figure 8.** General aspects of the copper mineralization I and II. (A) Disseminated chalcopyrite I associated with magnetite I and chlorite I. (B) Massive zone of chalcopyrite I with magnetite I and biotite II. (C) Chalcopyrite I-related silicification II zones and (D) granitic apophyses. (E) Massive chalcopyrite II ± bornite II associated with silicification II zones. (F) Main ore paragenesis (chalcopyrite I+magnetite I) associated with chlorite zones. (G) Octahedral magnetite I crystals with chalcopyrite I. (H) Stilpnomelane needles included in chalcopyrite I. (I) Chalcopyrite I+pyrite I in silicified I domains. (J) Idioblastic granular chalcopyrite II in silicified II zones associated with granitic apophyses. (K) Dendritic covellite with inclusions of cobaltite replacing bornite II. (L) Bornite III in hematite I hydrothermal breccias. (M) and (N) Bornite III replacing chalcopyrite III associated with specular hematite I in hydrothermal breccias. Images F, G, I, J, L, and M are photomicrographs under reflected light and plane-polarized light. Images H, K, and N are SEM backscattered electron images.

from 0.70 to 1.31, in relation to AN-34. Al/(Al+Mg+Fe) ratios show a small variation (0.33–0.39 at AN-34 and 0.24–0.37 at QT-02). Chlorine and fluorine contents in both chlorites are low, < 0.03 apfu and < 0.07 apfu, respectively.

In this paper, several geothermometers were applied to obtain the temperature formation of AN-34 and QT-02 chlorite and included those from Cathelineau and Nieva (1985), Jowett (1991), Kranidiotis and MacLean (1987), and Zang and Fyfe

**Table 1.** Representative EPMA analyses of chlorite from the AN-34 and QT-02 prospects.

Prospect	AN-34					QT-02		
Sample	DH0003_143					FD007_175		
Assemblage /Rock	Mineralization I (Ccp I ± Bn I + Mag I + Chl I ± Qtz I)					Banded iron formation		
Mineral	Chlorite I					Chlorite II		
SiO <sub>2</sub>	24.81	25.03	24.57	24.77	25.22	24.41	25.50	27.68
TiO <sub>2</sub>	0.03	0.05	0.02	0.05	0.04	0.03	0.05	0.37
Al <sub>2</sub> O <sub>3</sub>	20.24	19.91	19.48	20.45	20.27	19.72	19.76	17.03
Cr <sub>2</sub> O <sub>3</sub>	0.06	0.15	0.01	0.03	0.01	0.03	0.05	0.02
FeO	29.63	29.60	30.44	28.86	28.40	29.69	31.14	29.18
MnO	0.30	0.35	0.42	0.23	0.41	0.50	0.58	0.48
NiO	0.00	0.00	0.04	0.08	0.02	0.00	0.04	0.01
ZnO	0.00	0.00	0.03	0.07	0.00	0.05	0.00	0.02
MgO	10.70	10.94	10.31	11.14	12.37	11.08	10.99	10.29
CaO	0.13	0.05	0.03	0.08	0.03	0.07	0.05	0.07
Na <sub>2</sub> O	0.07	0.10	0.04	0.13	0.06	0.07	0.09	0.10
K <sub>2</sub> O	0.12	0.10	0.05	0.06	0.02	0.08	0.12	2.34
F	0.02	0.09	0.17	0.14	0.00	0.09	0.00	0.06
Cl	0.05	0.02	0.01	0.06	0.05	0.08	0.07	0.19
O=F	0.01	0.04	0.07	0.06	0.00	0.04	0.00	0.03
O=Cl	0.01	0.00	0.00	0.01	0.01	0.02	0.02	0.04
Total	86.18	86.43	85.69	86.22	86.91	85.96	88.46	87.91
Number of ions on the basis of 14 O								
Si	2.7396	2.7574	2.7527	2.7283	2.7370	2.7173	2.7624	3.0303
Ti	0.0025	0.0041	0.0017	0.0041	0.0033	0.0025	0.0041	0.0305
Al	2.6340	2.5850	2.5722	2.6547	2.5926	2.5872	2.5229	2.1973
Cr	0.0052	0.0131	0.0009	0.0026	0.0009	0.0026	0.0043	0.0017
Fe <sup>2+</sup>	2.7362	2.7270	2.8521	2.6583	2.5775	2.7640	2.8212	2.6715
Mn	0.0281	0.0327	0.0399	0.0215	0.0377	0.0471	0.0532	0.0445
Ni	0.0000	0.0000	0.0036	0.0071	0.0017	0.0000	0.0035	0.0009
Zn	0.0000	0.0000	0.0025	0.0057	0.0000	0.0041	0.0000	0.0016
Mg	1.7614	1.7966	1.7220	1.8292	2.0013	1.8387	1.7748	1.6793
Ca	0.0154	0.0059	0.0036	0.0094	0.0035	0.0083	0.0058	0.0082
Na	0.0150	0.0214	0.0087	0.0278	0.0126	0.0151	0.0189	0.0212
K	0.0169	0.0141	0.0071	0.0084	0.0028	0.0114	0.0166	0.3268
F	0.0070	0.0315	0.0604	0.0490	0.0000	0.0317	0.0000	0.0207
Cl	0.0094	0.0038	0.0019	0.0112	0.0092	0.0151	0.0129	0.0352
OH	7.9836	7.9648	7.9377	7.9398	7.9908	7.9532	7.9871	7.9441
Total	17.9543	17.9574	17.9670	17.9571	17.9709	17.9983	17.9877	18.0138
Fe/(Fe+Mg)	0.6084	0.6028	0.6235	0.5924	0.5629	0.6005	0.6138	0.6140
Fe(total)	2.7362	2.7270	2.8521	2.6583	2.5775	2.7640	2.8212	2.6715

(1995). The calculated temperatures vary from 246 to 394°C in AN-34 and 231 to 370°C in QT-02 (Fig. 9D). No drastic variances are observed among the different authors and proposed methods. We also show the R2+ vs. Si (apfu) diagram for chlorite from the AN-34 and QT-02 prospects. Chlorite from both deposits displays Tschermak as the main chlorite substitution along the clinocllore (Daphinite)–Amesite end-member line and plots around the zero vacancy line (Fig. 9E).

## 7 OXYGEN ISOTOPE COMPOSITION OF HYDROTHERMAL MINERALS

The oxygen isotope composition of the main hydrothermal alteration minerals at AN-34 and QT-02 were analyzed to constrain the ore-forming fluid evolution (Table 2). Analyses on quartz II ( $\delta^{18}\text{O}_{\text{VSMOW}} = 8.3\text{--}9.1\text{‰}$ ,  $n = 02$ ) and hematite II ( $\delta^{18}\text{O}_{\text{VSMOW}} = -9.0\text{‰}$ ,  $n = 01$ ) were carried out in AN-34. At QT-02, in contrast, the isotopic analyses were developed



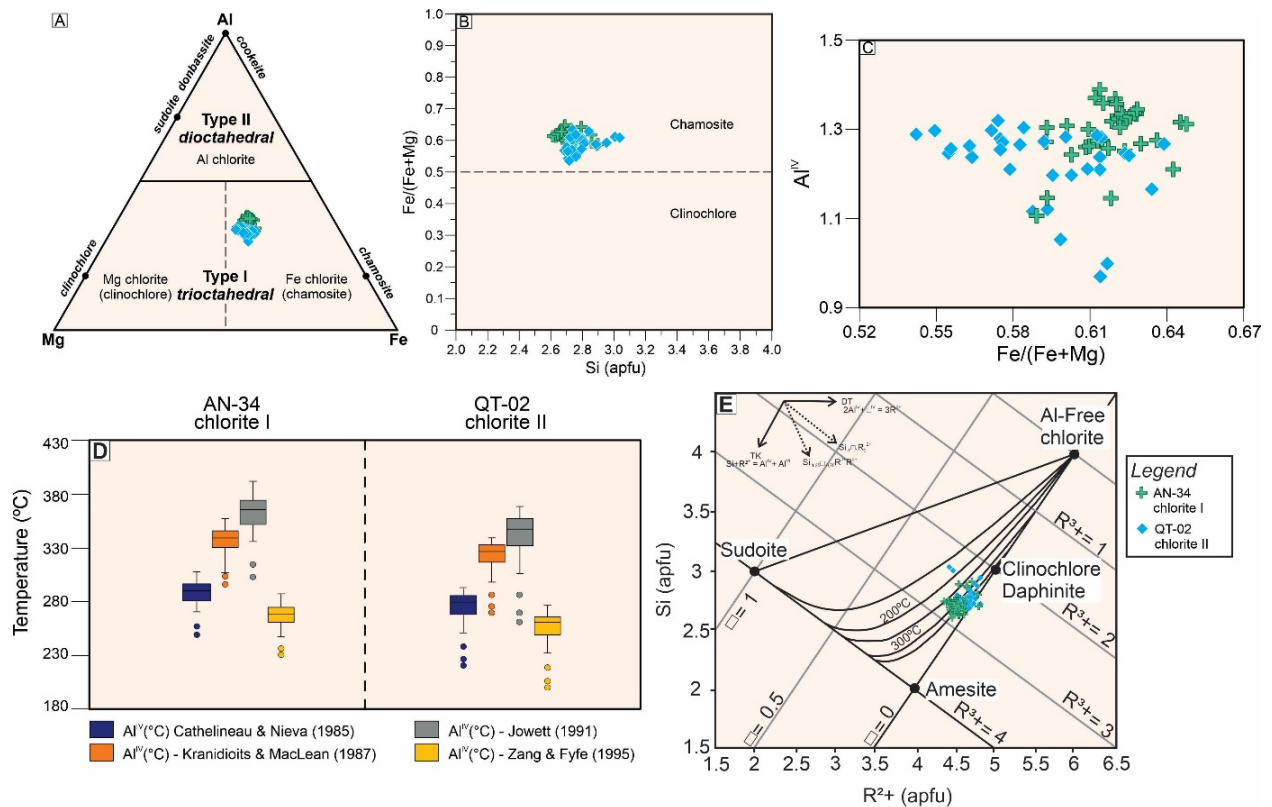


**Figure 9.** (A) Compositional variation of chlorite from the AN-34 and QT-02 prospects (Zane & Weiss, 1998) showing chamosite composition with richer Fe terms. (B) Chlorite distinction graph based on Fe/(Fe+Mg) and Si (apfu) content by Ruiz Cruz and Nieto (2006). (C) Relationship between Al<sup>IV</sup> content and Fe/(Fe+Mg)-to-chlorite ratio from the AN-34 and QT-02 prospects. (D) Boxplot showing values of chlorite crystallization temperature in the AN-34 and QT-02 prospects, according to the calibrations of Cathelineau and Nieva (1985), Jowett (1991), Kranidiotis and MacLean (1987), and Zang and Fyfe (1995). (E) Chlorite from the QT-02 and AN-34 deposits plotted in the R<sup>2+</sup> vs. Si (apfu) diagram (Wiewióra & Weiss, 1990) with isotherms calculated based on the study by Bourdelle and Cathelineau (2015).

**Table 2.** Oxygen isotope composition of distinct minerals and associated hydrothermal fluids from the AN-34 and QT-02 prospects.

Prospect	Sample no.	Hydrothermal alteration	Mineral	$\delta^{18}\text{O}_{\text{min}}$	T (°C)	$\delta^{18}\text{O}_{\text{H}_2\text{O}}$
AN-34	DH03/174,60	Silicification II (Mineralization II)	Quartz	9.1	520 ± 30	6.6 ± 0.29
	DH03/296,00	Late hematite vein	Hematite	-9.0	273 ± 20	1.7 ± 0.21
	DH05/305,90	Silicification II (Mineralization II)	Quartz	8.3	520 ± 30	5.8 ± 0.29
QT-02	FD04/284,00	Late hematite breccia	Hematite	-7.4	273 ± 20	3.3 ± 0.21
	FD04/302,05	Na alteration	Albite	7.1	273 ± 20	0.27 ± 0.68
	FD04/362,20	Na alteration	Albite	7.6	273 ± 20	0.77 ± 0.38
	FD07/193,40	Fe-enrichment	Quartz	11.7	520 ± 30	9.2 ± 0.29
	FD07/193,40	Fe-enrichment	Magnetite	1.2	520 ± 30	7.25 ± 0.17
	FD07/272,40	Fe-enrichment	Quartz	13.0	520 ± 30	10.47 ± 0.29
	FD07/272,40	Fe-enrichment	Magnetite	4.0	520 ± 30	10.05 ± 0.17

using quartz I ( $\delta^{18}\text{O}_{\text{VSMOW}} = 11.7\text{--}13.0\text{‰}$ , n = 02), magnetite I ( $\delta^{18}\text{O}_{\text{VSMOW}} = 1.2\text{--}4.0\text{‰}$ , n = 02), albite I ( $\delta^{18}\text{O}_{\text{VSMOW}} = 7.1\text{--}7.6\text{‰}$ , n = 02), and hematite II ( $\delta^{18}\text{O}_{\text{VSMOW}} = -7.4\text{‰}$ , n = 01).

## 7.1 Temperature and oxygen isotopic composition of the associated hydrothermal fluids

The quartz–magnetite pair was used to calculate the temperature, according to the oxygen isotope fractionation factors of Matthews et al. (1983). In addition, chlorite temperature

was calculated using mineral chemistry from EPMA obtained in this study. Two quartz–magnetite pairs provided a temperature of 550 and 490°C for Fe-enriched zones with magnetite I+quartz I at QT-02. Pervasive chlorite I showed a mean temperature of 287°C in AN-34 and late chlorite II of 273°C in QT-02, both obtained by chlorite geothermometer proposed by Cathelineau and Nieva (1985).

The temperature of 520°C represents the mean temperature value obtained for the quartz–magnetite pair from the Fe enrichment stage at QT-02. An interval of 30°C was chosen to

calculate the oxygen isotope composition of the fluid in equilibrium with the hydrothermal minerals. The temperature of 273°C, obtained from QT-02 chlorite, is associated with minerals related to ductile-brittle deformation linked to the final stage of the hydrothermal Cururu system. In this case, an interval of 20°C was applied to calculate the oxygen isotope composition of the fluid. These data are summarized in Table 3.

The oxygen isotope composition of the hydrothermal fluids ( $\delta^{18}\text{O}_{\text{H}_2\text{O}}$ ) was calculated using temperature intervals estimated for each hydrothermal alteration stage and isotopic fractionation factors for quartz-H<sub>2</sub>O (Clayton et al., 1972), magnetite-H<sub>2</sub>O (Bottinga & Javoy, 1973), albite-H<sub>2</sub>O (O'Neil & Taylor Jr., 1967), and hematite-H<sub>2</sub>O (Zheng, 1991).

In QT-02, fluids in equilibrium with quartz I and magnetite I associated with the Fe enrichment stage at 520°C display  $\delta^{18}\text{O}_{\text{H}_2\text{O}} = 9.2\text{‰}$ , 10.47‰ (quartz I) and  $\delta^{18}\text{O}_{\text{H}_2\text{O}} = 7.25\text{‰}$ , 10.05‰ (magnetite I) values. At the same temperature interval, fluids associated with silicification II have  $\delta^{18}\text{O}_{\text{H}_2\text{O}}$  values of 6.6 and 5.8‰. Fluids in equilibrium with sodic alteration at  $273^\circ\text{C} \pm 20^\circ\text{C}$  present  $\delta^{18}\text{O}_{\text{H}_2\text{O}} = 5.4$  and 5.9‰ (albite I) values. Also, fluids associated with hematite II present values of  $\delta^{18}\text{O}_{\text{H}_2\text{O}} = 1.7\text{‰}$  at AN-34 and 3.3‰ at QT-02.

## 8 DISCUSSION

### 8.1 Fluid–rock interaction and changes in the host rocks

The superposition of different styles/episodes of IOCG mineralization in the deposit scale is a common feature in the CD and worldwide (Skirrow et al., 2022, and references therein). Along the Cinzento Shear Zone, magmatic, deformational, and hydrothermal events overlap most of the original features of the host rocks of the IOCG deposits (e.g., Jesus, 2016; Salobo and Furnas; Melo et al., 2017). However, in the AN-34 and QT-02 prospects, the host rocks are relatively preserved when compared to other deposits in the region (e.g., Salobo and Furnas deposits), and the transition toward hydrothermally altered lithotypes is clearly seen.

These prospects are chiefly hosted by BIFs and basic volcanic rocks with preserved primary structures (i.e., primary bedding and amygdaloidal texture). These rocks are only affected by dynamic metamorphism due to the shearing of the Cinzento Shear Zone, but no regional metamorphism was observed. Regional metamorphism over Neoproterozoic rocks has been ruled out in the region by some authors (e.g., Hunger et al., 2018; Melo et al., 2017). However, dynamic

metamorphism has strongly affected the country rocks along the Cinzento Shear Zone (Toledo et al., 2023). Although geochronological data have not been obtained for the area, the rocks of the Cururu Region can be attributed to the metavolcanic sedimentary units of the Salobo-Pojuca Formation and Itacaiúnas Supergroup (2.76–2.73 Ga). The age of the granitic rocks, however, remains unknown, but it might be from the widespread Neoproterozoic granite magmatism (2.76–2.73 Ga; e.g., Toledo et al., 2023) or of Paleoproterozoic age (1.88 Ga; Vasquez et al., 2008).

Though there are small differences between both prospects, they seem to have evolved from the same ore-forming fluid. The hierarchy of hydrothermal paragenesis allowed us to identify an initial stage of pervasive silicification. Following this alteration, Fe enrichment (magnetite I+grunerite+almandine) and potassic alteration with biotite, associated with shearing development, are ubiquitous at the prospect. Fe enrichment and potassic alteration are also widespread in other IOCG deposits of the region, including Salobo, GT-46, Grota Funda, and Furnas (e.g., Hunger et al., 2018; Melo et al., 2017).

The mineralization I encompasses the main mineralization stage at the Cururu Region, and it is represented by elongated sheared lenses composed of chalcopyrite I+magnetite I ± bornite I ± pyrite coeval to potassic alteration and syn-shearing. Minor occurrences of uraninite, Y-xenotime, allanite, apatite, and cobaltite related to mineralization II reflect associations with U, REE, and Co. The second stage of silicification (i.e., quartz II) is coeval to the second episode of copper precipitation. The mineralization II with chalcopyrite II+quartz II ± bornite II usually occurs close to granitic apophysis. This ore mineralogy can be associated with the geochemical signatures of the ore zones likely related to the Neoproterozoic ores of the northern sector of the CD (Carneiro et al., 2023).

Chlorite I formation is the most pervasive alteration, syn- to post-mineralization I, in both prospects. Chlorite alteration zones are characteristic of shallow crustal level deposits, like Sossego, Alvo 118, and Grota Funda (Hunger et al., 2018; Monteiro et al., 2008; Torresi et al., 2012), representing the latest cool stages of the hydrothermal systems.

The transition from an essentially ductile to a ductile-brittle regime can be observed with the development of a pervasive sodic alteration (albite I) at the QT-02 prospect. This alteration is poorly observed in the hydrothermal paragenesis at deposits of the northern sector. A ductile-brittle regime with breccias, veins, veinlets, and stockwork zones followed the intense chloritic alteration and sodic alteration. Hydrothermal breccias with specular hematite II+biotite III-rich matrix occur in

**Table 3.** Temperatures estimated from oxygen isotope composition and mineral chemistry from the AN-34 and QT-02 prospects.

Prospect	Mineral	Hydrothermal alteration	Oxygen isotopes	Mineral chemistry
AN-34	Chlorite I	Pervasive chloritization		287°C (Chlorite geothermometer)
QT-02	Quartz I + Magnetite I	Fe-enrichment	550°C (Qtz-Mag pair)	
			490°C (Qtz-Mag pair)	
			Mean = 520 ± 30°C	
	Chlorite II	Late veins		273 ± 20°C (Chlorite geothermometer)



granitoids in QT-02. In addition to the brittle regime being represented by hematite II rich-breccias, veins and veinlets cut the hydrothermal lithotype sequence and granitoids. Also, chalcopyrite IV (mineralization IV) occurs mainly in quartz III, carbonate, and albite II veins and veinlets, similar to those described in the Gameleira deposit, of Paleoproterozoic age (Lindenmayer et al., 2001).

## 8.2 Origin of the ore-forming fluids and temperature

The hydrothermal alteration halos at AN-34 and QT-02 point to a decrease in the temperature. This is evidenced by hydrothermal alteration assemblages and confirmed by oxygen-stable isotopes and chlorite geothermometry.

The isotopic temperature in the QT-02 prospect obtained by the quartz–magnetite pair is quite similar to that calculated for the quartz–biotite pair at the Salobo deposit of  $565^{\circ}\text{C} \pm 50^{\circ}\text{C}$  for Fe enrichment and potassic alteration (Melo et al., 2019). These temperature conditions might be very similar at the early stages of AN-34 as well.  $\delta^{18}\text{O}_{\text{H}_2\text{O}}$  values for the hydrothermal fluids in equilibrium with Fe enrichment ( $7.25\text{--}10.47\text{‰}$ ), silicification II ( $5.8\text{--}6.6\text{‰}$ ) at  $520^{\circ}\text{C} \pm 30^{\circ}\text{C}$ , indicating an essentially magmatic source for the fluids (Fig. 10). Magmatic fluids were documented as the main fluids in the IOCG deposits from the northern sector and Southern Copper Belt of Carajás (Melo et al., 2019; Monteiro et al., 2008; Pestilho et al., 2020).

The widespread pervasive chlorite I formation is the latest stage of hydrothermal alteration in a ductile stage. At the

Salobo deposit, the temperature of syn- to post-mineralization chlorite is  $347^{\circ}\text{C}$  (Réquia, 1995). However, Zang and Fyfe (1995) suggest that the hydrothermal processes involved chlorite occurred at a range of  $200\text{--}270^{\circ}\text{C}$  at the Igarapé Bahia deposit. The Furnas deposit, in turn, presented a wide temperature range for chlorite formation, which must be interpreted with caution ( $225\text{--}425^{\circ}\text{C}$ ; Jesus, 2016).

Values for  $\delta^{18}\text{O}_{\text{H}_2\text{O}}$  between  $1.55$  and  $3.15\text{‰}$  for hematite-rich breccias associated with mineralization III were calculated at  $273^{\circ}\text{C} \pm 20^{\circ}\text{C}$  based on chlorite geothermometer. This is linked to a low-temperature stage that takes place at the later stages of the hydrothermal system due to interaction with externally derived fluids depleted in  $^{18}\text{O}$  (Fig. 10). This alteration of a ductile to ductile-brittle deformation regime and late interaction of fluids with different sources was also observed at Sossego, Alvo 118, Salobo, and Igarapé Bahia deposits (Melo et al., 2019; Monteiro et al., 2008; Torresi et al., 2012).

The influence of high-temperature fluids (i.e., magmatic fluids) associated with the ductile deformation regime gave origin to specific temperature alterations, such as iron enrichment. Temperature conditions decay from  $520^{\circ}\text{C} \pm 30^{\circ}\text{C}$  (magnetite–quartz pair in Fe enrichment) to  $273^{\circ}\text{C} \pm 20^{\circ}\text{C}$  (chlorite geothermometer in pervasive chlorite I), which suggests a fluid mixing for ore precipitation. Conversely, the precipitation of minerals in breccias, veins, and veinlets (hematite II and chlorite II) points to a brittle regime and a different style of alteration. The source of fluids, the deformation regime, and the timing of this event must be interpreted with caution.

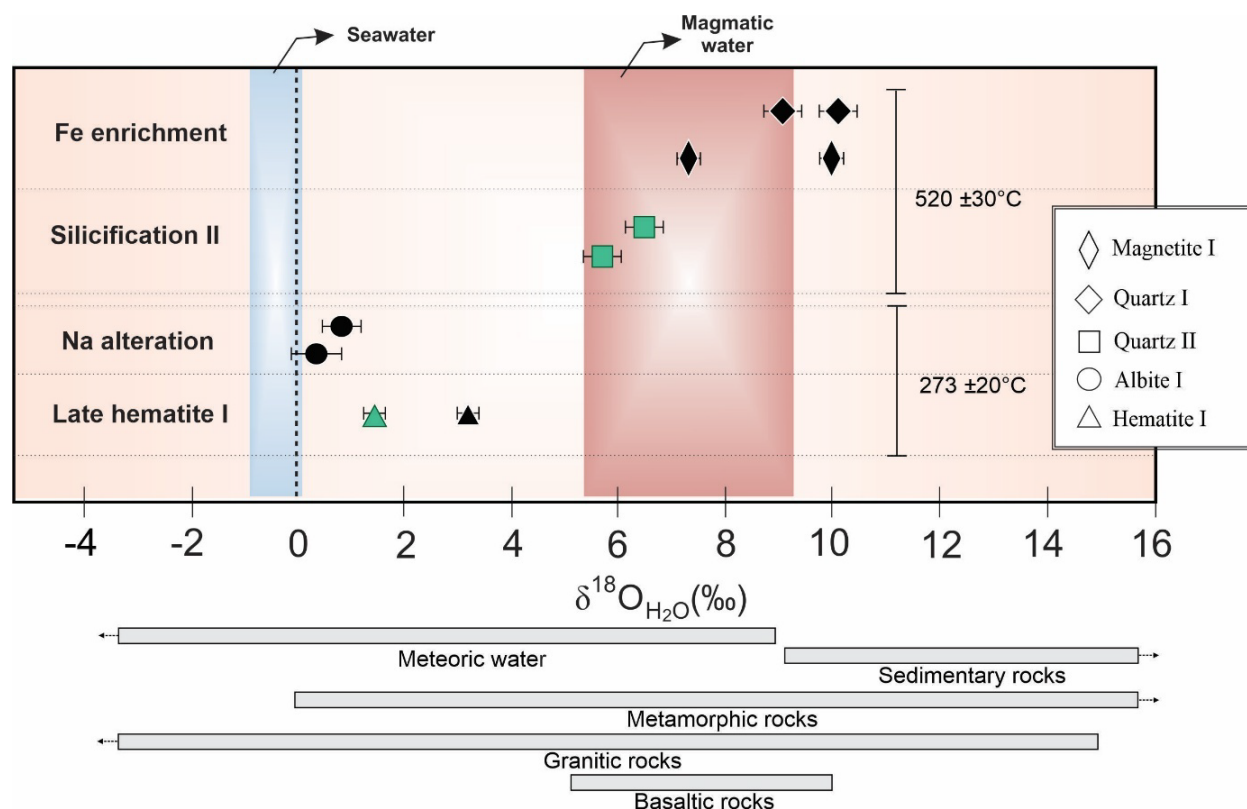


**Figure 10.** Oxygen isotope composition of hydrothermal fluids in equilibrium with silicates and oxides from the AN-34 (green symbol) and QT-02 (black symbol) prospects. Seawater and magmatic water fields are from Taylor Jr. (1997) and the distribution of  $\delta^{18}\text{O}$  values for meteoric water and sedimentary, metamorphic, granitic, and basaltic rocks obtained from Hoefs (2009).

### 8.3 The Cururu Region: Clues for a complex metallogenic evolution

The metallogenic evolution of the Cururu Region is very similar to that reported of the northern sector, like Salobo, Igarapé Bahia, Furnas, GT-46, and Grota Funda (Hunger et al., 2018; Jesus, 2016; Lindenmayer & Teixeira, 1999; Melo et al., 2017; Melo et al., 2019; Toledo et al., 2019). These similarities include early high-temperature hydrothermal alteration evolving to lower-temperature hydrothermal halos, copper mineralization associated with significant amounts of magnetite, and structural control of the hydrothermal alteration associated with the development and/or reactivation of Cinzento Shear Zone.

However, the hydrothermal alteration halos and the copper mineralization seem to be weaker and localized at these prospects. At the Cururu Region, chloritic alteration is stronger than that reported at Salobo, Furnas, and GT-46, suggesting an intense telescoping of the low-temperature hydrothermal system over the high-temperature assemblage (i.e., grunerite–almandine–biotite). Thus, with low temperature and low salinity, Cu-poor hydrothermal fluids in a shallower level were dominant in this region.

Almandine–grunerite (biotite)–magnetite-rich rocks have been broadly described at Salobo, GT-46, Furnas, and Grota Funda deposits. This mineral assemblage has been interpreted as metamorphic paragenesis, strongly obliterated by pervasive and recurring hydrothermal alteration stages at GT-46 and Furnas deposits (Jesus, 2016; Toledo et al., 2019). On the contrary, in Salobo and Grota Funda, they were assigned as hydrothermal alteration products due to intense fluid–rock interaction (Hunger et al., 2018; Melo et al., 2017). At these deposits, however, the fluid/rock ratio is high and the transitions from the unaltered host to almandine–grunerite (biotite)–magnetite-rich rocks are not clear. At the Cururu Region, geological evidence suggests a gradual transition from non-altered lithotypes to grunerite–magnetite–almandine–biotite-rich rocks, which is best seen at BIFs from the QT-02 prospect. Therefore, this mineral assemblage could also be assigned as a product of hydrothermal alteration, likely resulting from intense fluid/rock interaction and deformation. Grunerite–magnetite–almandine–biotite-rich rocks might be primary prospecting guides for copper mineralization along the Cinzento Shear Zone. Additionally, the strong Fe enrichment in AN-34 and QT-02 could be related to iron leaching from BIFs and, thus, BIFs might be a lithological control for the IOCG deposit along the Cinzento Shear Zone.

This paragenesis can be linked with IOCG episode at ca. 2.5 Ga, as reported for Salobo, Grota Funda, Furnas, and GT-46 (Hunger et al., 2018; Jesus, 2016; Melo et al., 2017; Melo et al., 2019; Toledo et al., 2019). The results of oxygen isotope composition at the Cururu Region evidence the importance of essentially magmatic fluids for the formation of copper ore. In the Salobo and Igarapé Bahia deposits, the isotopic results denote the influence of magmatic or metamorphic fluids for the genesis of the deposits (Melo et al., 2019). However, the late stages of the evolution of the system are associated with an externally derived source of fluids (Melo et al.,

2019). The link between Carajás IOCG deposits and granite magmatism remains unclear, although some authors state an obvious spatial relation between these deposits and magmatic intrusions (Groves et al., 2010; Pollard, 2006).

A diversity of granite plutons has been recently recognized in the deposit scale along the Cinzento Shear Zone. The ca. 2.5 Ga magmatism, represented by Old Salobo, Itacaiúnas, and undeformed granites at GT-46, is coeval with mineralization at Salobo, Igarapé Bahia, and GT-46 deposits (Machado et al., 1991; Melo et al., 2017; Réquia et al., 2003; Tallarico et al., 2005; Toledo et al., 2019). On the contrary, recent studies of trace elements in zircon suggested that these granitic bodies could be products of a regional intense fluid–rock interaction, in which fluids may have been derived from the mantle (Toledo et al., 2023). In this case, there would be no 2.5 Ga granite magmatism, and these ages would be hybrid ages caused by isotopic disturbances due to a regional hydrothermal event (Toledo et al., 2023).

Although not dated, the general aspects of host rocks at AN-34 and QT-02, including hydrothermal alteration patterns (grunerite–almandine–biotite), deformation features, and alteration-mineralization styles, suggest that this system may have formed at ca. 2.5 Ga. This is like the ages reported at Igarapé Bahia, Grota Funda, and Salobo IOCG deposits (Hunger et al., 2018; Réquia et al., 2003; Tallarico et al., 2005). However, the timing of mineralization in these prospects deserves more investigation, and overprint events cannot be ruled out.

Magmatic fluids were likely derived from deep-seated sources (i.e., mantle-plume derived) and ascended throughout translithospheric structures (Diniz et al., 2023; Teixeira et al., 2020; Toledo et al., 2023), though this possibility remains very speculative. Mantle-derived granites (Creaser et al., 1996) are also proposed for the genesis of the giant Olympic Dam (Courtney-Davies et al., 2020). At the Andean IOCG deposits, arc magmatism with fluid sources at depth has been deemed mainly responsible for IOCG genesis (Del Real et al., 2023; Rodriguez-Mustafa et al., 2022; Simon et al., 2018). However, at Carajás, the source of these fluids remains unknown and debatable.

The development of deformation zones and networks of deformation zones due to the Cinzento Shear Zone creates fundamental structures that control fluid circulation and copper mineralization (Blenkinsop et al., 2020; Xavier et al., 2012). As the fluid ascended through crustal-scale shear zones, the fluid–rock interaction increased and temperature decreased, which might have triggered the formation of the hydrothermal alteration halos and ore precipitation.

The change in structural regime from ductile to ductile-brittle and the participation of externally derived fluids are recorded at mineralization III in hydrothermal breccias. The interaction of external  $^{18}\text{O}$ -depleted fluids with primary magmatic fluids is observed in the northern sector as in the southern copper belt and assigned as the most important process for ore precipitation (Melo et al., 2019; Monteiro et al., 2008; Pestilho et al., 2020; Torresi et al., 2012; Silva et al., 2015). Nevertheless, the influence of Paleoproterozoic



granitic unit (e.g., 1.88 Ga, Cigano granite) emplacement as heat and metal sources in the Cururu Region cannot be ruled out. These younger granites could be responsible for another hydrothermal event as a source of heat that caused the development of shallow emplaced ore precipitation (mineralization IV) at the AN-34 and QT-02 prospects.

Hence, the Cururu Region, with the AN-34 and QT-02 prospects, has some pieces of a complex puzzle of copper metallogenesis in the northern sector of the CD. These prospects, though not important in terms of ore tonnage, are part of a wider mineral system at Carajás and share the same ore-forming processes with the larger deposits in the region (Skirrow et al., 2022).

## 9 CONCLUSIONS

Detailed characterization of the host rocks, hydrothermal alteration halos, ore zones aligned with mineral chemistry, and stable isotopes at the AN-34 and QT-02 prospects provided new insights for IOCG systems in the north of the CD:

- BIF, basic volcanic rocks, and granite units are the main host rocks in the Cururu Region. Intense hydrothermal alteration over these rocks originated from high-temperature mineral assemblages such as grunerite, almandine, and magnetite that evolves into mineral assemblages of lower temperature represented by chlorite, hematite, and sericite;
- Fe enrichment (grunerite+almandine+magnetite) identified in the Cururu area and in other IOCG deposits in the northern sector suggests a possible lithology over these deposits;
- Oxygen isotopes reveal fluids of magmatic origin with high temperatures ( $520^{\circ}\text{C} \pm 30^{\circ}\text{C}$ ) evolving to lower-temperature ( $273^{\circ}\text{C} \pm 20^{\circ}\text{C}$ ) meteoric fluids;
- Based on the hydrothermal alteration assemblages and development of ductile to ductile-brittle structural regime

associated with an increase in the  $f\text{O}_2$ , the AN-34 and QT-02 prospects may be considered an IOCG system with shallow-to-intermediate crustal-level evolution.

These findings shed light on the complex metallogenetic evolution of the northern CD. The prospects reveal changes in the mineralogy, texture, and deformation structures of the host rocks, as a result of the development of the hydrothermal system, whether through a long-lived process (e.g., the Salobo deposit; Melo et al., 2017) or via multiple stages (e.g., the GT-46 deposit; Toledo et al., 2019). These insights are crucial for advancing our understanding of IOCG mineral systems, as prospects and satellite targets around large, world-class deposits offer key clues to the underlying ore-forming processes. This can be seen in other important provinces, including the Gawler Catron (Australia: Wirrda Well and Acropolis deposits), at Great Bear Magmatic Zone (Canada: Nori and DeVries deposits; Kelly et al., 2020; Krneta et al., 2017). Thus, unraveling the metallogenetic evolution of these small deposits and prospects can help in the understanding of the ore-forming processes and the development of mineral exploration campaigns and enhance the cost-effectiveness of the area.

## ACKNOWLEDGMENTS

We are very grateful to the Vale Company, especially to Fernando Matos, Wolney Rosa, and Saney Freitas. We acknowledge the Microscopy and Microanalysis Laboratory of the UFOP (Brasil) and the Scottish Universities Environmental Research Center of the University of Glasgow (Scotland). This research was funded by the Fundação de Amparo à Pesquisa do Estado de São Paulo (FAPESP; 2016/13162-7) and Conselho Nacional de Desenvolvimento Científico e Tecnológico (CNPq; 429689/2018-7). The second author thanks CAPES for his scholarship during his master's.

## ARTICLE INFORMATION


Manuscript ID: 20240034. Received on: 23 JULY 2024. Approved on: 31 MAR 2025.

How to cite: Melo, G. H. C., Santos, B. C. S., Xavier, R. P., Moreto, C. P. N., Toledo, P. I. F., Nascimento, G. Q., Castro, M. P., & Paula, F. C. (2025). Fluid evolution and hydrothermal alteration in the AN-34 and QT-02 IOCG prospects: clues for IOCG metallogenesis in the northern sector of the Carajás Mineral Province, Amazonian Craton. *Brazilian Journal of Geology*, 55, e20240034. <https://doi.org/10.1590/2317-488920240034>

GHCM: Funding acquisition, investigation, methodology, project administration, supervision, validation, writing—original draft, writing—review and editing. BCSS: Conceptualization, data curation, investigation, writing—original draft, writing—review and editing. RPX: Funding acquisition, project administration, supervision, validation, writing—review and editing. CPNM: Funding acquisition, investigation, project administration, supervision, validation. PIFT: Conceptualization, data curation, investigation, writing—original draft. GQN: Methodology. MPC: Methodology. FCP: Investigation.

Competing interests: The authors declare no competing interests.

SCIENTIFIC EDITOR: Carlos Grohmann 

ASSOCIATE EDITOR: Adalene Moreira Silva 

## REFERENCES

- Araújo Filho, R. C., Nogueira, A. C. R., & Araújo, R. N. (2020). New stratigraphic proposal of a Paleoproterozoic siliciclastic succession: Implications for the evolution of the Carajás Basin, Amazonian craton, Brazil. *Journal of South American Earth Sciences*, 102, 102665. <https://doi.org/10.1016/J.JSAMES.2020.102665>
- Barbosa, J. P. O. (2004). *Geologia estrutural, geoquímica, petrografia e geocronologia de granitóides da região do Igarapé Gelado, norte da Província Mineral de Carajás*. [Dissertação de mestrado, Universidade Federal do Pará].

- Barros, C. E. M., Sardinha, A. S., De Barbosa, J. D. P. O., Macambira, M. J. B., Barbey, P., & Boullier, A. M. (2009). Structure, petrology, geochemistry and zircon U/Pb and Pb/Pb geochronology of the synkinematic archaic (2.7 Ga) A-type granites from the Carajás Metallogenic Province, northern Brazil. *The Canadian Mineralogist*, 47, 1423-1440. <https://doi.org/10.3749/CANMIN.47.6.1423>
- Blenkinsop, T. G., Oliver, N. H. S., Dirks, P. G. H. M., Nugus, M., Tripp, G., & Sanislav, I. (2020). Structural geology applied to the evaluation of hydrothermal gold deposits. In J. V. Rowland & D. A. Rhys (Eds.), *Reviews in Economic Geology: applied structural geology of ore-forming hydrothermal systems*. Society of Economic Geologists. <https://doi.org/10.5382/rev.21.01>
- Bottinga, Y., & Javoy, M. (1973). Comments on oxygen isotope geothermometry. *Earth Planet Science Letters*, 20(2), 250-265. [https://doi.org/10.1016/0012-821X\(73\)90165-9](https://doi.org/10.1016/0012-821X(73)90165-9)
- Bourdelle, F., & Cathelineau, M. (2015). Low-temperature chlorite geothermometry: a graphical representation based on a T-R2+-Si diagram. *European Journal of Mineralogy*, 27(5), 617-626. <https://doi.org/10.1127/ejm/2015/0027-2467>
- Carneiro, L. S., Moreto, C. P. N., Monteiro, L. V. S., & Xavier, R. P. (2023). Geochemical signatures of the Neoproterozoic and Paleoproterozoic copper systems in the Carajás Mineral Province, NW Brazil: Implications for metal endowment. *Journal of Geochemical Exploration*, 254, 107306. <https://doi.org/10.1016/j.jgexplo.2023.107306>
- Cathelineau, M., & Nieva, D. (1985). A chlorite solid solution geothermometer. The Los Azufres (Mexico) geothermal system. *Contributions to Mineralogy and Petrology*, 91, 235-244. <https://doi.org/10.1007/BF00413350>
- Clayton, R. N., O'Neil, J. R., & Mayeda, T. K. (1972). Oxygen isotope exchange between quartz and water. *Journal Geophysical Research*, 77(17), 3057-3067. <https://doi.org/10.1029/JB077i017P03057>
- Corriveau, L., Montreuil, J. F., & Potter, E. G. (2016). Alteration facies linkages among iron oxide copper-gold, iron oxide-apatite, and affiliated deposits in the great bear magmatic zone, northwest territories, Canada. *Economic Geology*, 111, 2045-2072. <https://doi.org/10.2113/ECONGEO.111.8.2045>
- Costa, U. A. P., Paula, R. R., Silva, D. P. B., Barbosa, J. P. O., Silva, C. M. G., Tavares, F. M., Oliveira, J. K. M., & Justo, A. P. (2016). *Mapa de integração geológico-geofísica da ARIM Carajás: Estado do Pará*. CPRM. Escala 1:250.000.
- Courtney-Davies, L., Ciobanu, C. L., Tapster, S. R., Cook, N. J., Ehrig, K., Crowley, J. L., Verdugo-Ihl, M. R., Wade, B. R., & Condon, D. J. (2020). Opening the magmatic-hydrothermal window: high-precision U-Pb geochronology of the Mesoproterozoic Olympic Dam Cu-U-Au-Ag deposit, South Australia. *Economic Geology*, 115(8), 1855-1870. <https://doi.org/10.5382/econgeo.4772>
- Creaser, R. A. (1996). Petrogenesis of a Mesoproterozoic quartz latite-granitoid suite from the Roxby Downs area, South Australia. *Precambrian Research*, 79(3-4), 371-394. [https://doi.org/10.1016/S0301-9268\(96\)00002-2](https://doi.org/10.1016/S0301-9268(96)00002-2)
- Del Real, I., Reich, M., Simon, A. C., Deditius, A., Barra, F., Rodríguez-Mustafa, M. A., Thompson, J. F. H., & Roberts, M. P. (2023). Formation of giant iron oxide-copper-gold deposits by superimposed episodic hydrothermal pulses. *Scientific Reports*, 13(1), 12041. <https://doi.org/10.1038/s41598-023-37713-w>
- DOCEGEO (1988). *Revisão litostratigráfica da Província Mineral de Carajás – litostratigrafia e principais depósitos minerais*. In 35º Congresso Brasileiro de Geologia, Belém.
- Feio, G. R. L., Dall'Agnol, R., Dantas, E. L., Macambira, M. J. B., Gomes, A. C. B., Sardinha, A. S., Oliveira, D. C., Santos, R. D., & Santos, P. A. (2012). Geochemistry, geochronology, and origin of the Neoproterozoic Planalto Granite suite, Carajás, Amazonian craton: A-type or hydrated charnockitic granites? *Lithos*, 151, 57-73. <https://doi.org/10.1016/j.lithos.2012.02.020>
- Groves, D. I., Bierlein, F. P., Meinert, L. D., & Hitzman, M. W. (2010). Iron oxide copper-gold (IOCG) deposits through Earth history: Implications for origin, lithospheric setting, and distinction from other epigenetic iron oxide deposits. *Economic Geology*, 105(3), 641-654. <https://doi.org/10.2113/gsecongeo.105.3.641>
- Guggenheim, S., Adams, J. M., Bain, D. C., Bergaya, F., Brigatti, M. F., Drits, V. A., Formoso, M. L. L., Galán, E., Kogure, T., & Stanjek, H. (2006). Summary of recommendations of nomenclature committees relevant to clay mineralogy: Report of the Association Internationale pour l'Etude des Argiles (AIPEA) nomenclature committee for 2006. *Clays and Clay Minerals*, 54(6), 761-772. <https://doi.org/10.1346/CCMN.2006.0540610>
- Hitzman, M. W. (2000). Iron oxide–Cu–Au deposits: what, where, when, and why. In T. M. Porter (Ed.), *Hydrothermal iron oxide copper-gold and related deposits: a global perspective*. Austral Miner Fund.
- Hoefs, J. (2009). *Stable isotope geochemistry* (Vol. 285). Springer.
- Hunger, R. B., Xavier, R. P., Moreto, C. P. N., & Gao, J. F. (2018). Hydrothermal alteration, fluid evolution, and re-os geochronology of the grota funda iron oxide copper-gold Deposit, Carajás Province (Pará State), Brazil. *Economic Geology*, 113(8), 1769-1794. <https://doi.org/10.5382/ECONGEO.2018.4612>
- Jesus, S. S. G. P. (2016). *Múltiplos estágios de alteração hidrotermal do depósito de óxido de ferro-cobre-ouro Furnas, Província Carajás: evolução paragenética e química mineral* [Dissertação de mestrado, Universidade de São Paulo].
- Jowett, E. C. (1991). Fitting iron and magnesium into the hydrothermal chlorite geothermometer. In Proceedings of the Program with Abstracts, Geological Association of Canada – Mineralogical Association of Canada, Society of Economic Geologists, 16, A62.
- Kelly, C. J., Davis, W. J., Potter, E. G., & Corriveau, L. (2020). Geochemistry of hydrothermal tourmaline from IOCG occurrences in the Great Bear magmatic zone: Implications for fluid source(s) and fluid composition evolution. *Ore Geology Reviews*, 118, 103329. <https://doi.org/10.1016/J.OREGEOREV.2020.103329>
- Kranidiotis, P., & MacLean, W. H. (1987). Systematics of chlorite alteration at the Phelps Dodge massive sulfide deposit, Matagami, Quebec. *Economic Geology*, 82, 1898-1911. <https://doi.org/10.2113/GSECONGEO.82.7.1898>
- Krnet, S., Cook, N. J., Ciobanu, C. L., Ehrig, K., & Kontonikas-Charos, A. (2017). The Wirra Well and Acropolis prospects, Gawler Craton, South Australia: Insights into evolving fluid conditions through apatite chemistry. *Journal of Geochemical Exploration*, 181, 276-291. <https://doi.org/10.1016/J.GEXPLO.2017.08.004>
- Lindenmayer, Z. G., & Teixeira, J. B. G. (1999). Ore genesis at the Salobo copper deposit, Serra dos Carajás. In M. G. Silva & A. Misi (Eds.), *Base metal deposits of Brazil* (pp. 33-43). Ministério de Minas e Energia (MME)/ Companhia de Pesquisa de Recursos Minerais (CPRM)/ Departamento Nacional de Produção Mineral (DNPM).
- Lindenmayer, Z. G., Pimentel, M. M., Ronchi, L. H., Althoff, F. J., Laux, J. H., Araújo, J. C., & Nowatzki, A. C. (2001). Geologia do depósito de Cu–Au de Gameleira, Serra dos Carajás, Pará. In DNPM-ADIMB (Ed.), *Depósitos auríferos dos distritos mineiros brasileiros* (pp. 79-137). DNPM-ADIMB.
- Machado, N., Lindenmayer, D. H., Krough, T. E., & Lindenmayer, Z. G. (1991). U-Pb geochronology of Archean magmatism and basement reactivation in the Carajás area, Amazon Shield, Brazil. *Precambrian Research*, 49(3-4), 329-354. [https://doi.org/10.1016/0301-9268\(91\)90040-H](https://doi.org/10.1016/0301-9268(91)90040-H)
- Martins, P. L. G., Toledo, C. L. B., Silva, A. M., Chemale Jr., F., Santos, J. O. S., Assis, L. M. (2017). Neoproterozoic magmatism in the southeastern Amazonian Craton, Brazil: Petrography, geochemistry and tectonic significance of basalts from the Carajás Basin. *Precambrian Research*, 302, 340-357. <https://doi.org/10.1016/j.precamres.2017.10.013>
- Matthews, A., Goldsmith, J. R., & Clayton, R. N. (1983). Oxygen isotope fractionations involving pyroxenes: The calibration of mineral-pair geothermometers. *Geochimica et Cosmochimica Acta*, 47(3), 631-644. [https://doi.org/10.1016/0016-7037\(83\)90284-3](https://doi.org/10.1016/0016-7037(83)90284-3)
- Melo, G. H. C., Monteiro, L. V. S., Xavier, R. P., Moreto, C. P. N., & Santiago, E. (2019). Tracing Fluid Sources for the Salobo and Igarapé Bahia Deposits: Implications for the Genesis of the Iron Oxide Copper-Gold Deposits in the Carajás Province, Brazil. *Economic Geology*, 114(4), 697-718. <https://doi.org/10.5382/ECONGEO.4659>
- Melo, G. H. C., Monteiro, L. V. S., Xavier, R. P., Moreto, C. P. N., Santiago, E. S. B., Dufrane, S. A., Aires, B., & Santos, A. F. F. (2017). Temporal evolution of the giant Salobo IOCG deposit, Carajás Province (Brazil): constraints from paragenesis of hydrothermal alteration and U-Pb geochronology. *Mineralium Deposita*, 52, 709-732. <https://doi.org/10.1007/S00126-016-0693-5>
- Monteiro, L. V. S., Xavier, R. P., Carvalho, E. R., Hitzman, M. W., Johnson, C. A., Souza Filho, C. R., & Torresi, I. (2008). Spatial and temporal zoning of hydrothermal alteration and mineralization in the Sossego iron oxide-copper-gold deposit, Carajás Mineral Province, Brazil: Paragenesis and stable isotope constraints. *Mineralium Deposita*, 43, 129-159. <https://doi.org/10.1007/s00126-006-0121-3>
- Moreto, C. P. N., Monteiro, L. V. S., Xavier, R. P., Creaser, R. A., Dufrane, S. A., Melo, G. H. C., Delinardo da Silva, M. A., Tassinari, C. C. G., & Sato, K. (2015a). Timing of multiple hydrothermal events in the iron oxide–copper–gold deposits of the Southern Copper Belt, Carajás Province, Brazil. *Mineralium Deposita*, 50, 517-546. <https://doi.org/10.1007/S00126-014-0549-9>



- Moreto, C. P. N., Monteiro, L. V. S., Xavier, R. P., Creaser, R. A., DuFrane, S. A., Tassinari, C. C. G., Sato, K., Kemp, A. I. S., & Amaral, W. S. (2015b). Neoproterozoic and paleoproterozoic iron oxide-copper-gold events at the Sossego Deposit, Carajás Province, Brazil: Re-Os and U-Pb geochronological evidence. *Economic Geology*, 110(3), 809-835. <https://doi.org/10.2113/ECONGEO.110.3.809>
- O'Neil, J. R., & Taylor Jr., H. P. (1967). The oxygen isotope and cation exchange chemistry of feldspars. *American Mineralogist*, 52(9-10), 1414-1437.
- Pestillo, A. L. S., Monteiro, L. V. S., Melo, G. H. C. de, Moreto, C. P. N., Juliani, C., Fallick, A. E., & Xavier, R. P. (2020). Stable isotopes and fluid inclusion constraints on the fluid evolution in the Bacaba and Castanha iron oxide-copper-gold deposits, Carajás Mineral Province, Brazil. *Ore Geology Reviews*, 126, 103738. <https://doi.org/10.1016/j.OREGEOREV.2020.103738>
- Pollard, P. J. (2006). An intrusion-related origin for Cu-Au mineralization in iron oxide-copper-gold (IOCG) provinces. *Mineralium Deposita*, 41, 179-187. <https://doi.org/10.1007/S00126-006-0054-X>
- Réquia, K. (1995). O papel do metamorfismo e fases fluidas na gênese da mineralização de cobre de Salobo, Província Mineral de Carajás, Pará. [Mestrado, Universidade Estadual de Campinas].
- Réquia, K., Stein, H., Fontboté, L., & Chiaradia, M. (2003). Re-Os and Pb-Pb geochronology of the Archean Salobo iron oxide copper-gold deposit, Carajás mineral province, northern Brazil. *Mineralium Deposita*, 38, 727-738. <https://doi.org/10.1007/S00126-003-0364-1>
- Rodriguez-Mustafa, M. A., Simon, A. C., Bilenker, L. D., Bindeman, L., Mathur, R., & Machado, E. L. (2022). The Mina Justa iron oxide copper-gold (IOCG) deposit, Peru: constraints on metal and ore fluid sources. *Economic Geology*, 117(3), 645-666. <https://doi.org/10.5382/econgeo.4875>
- Ruiz Cruz, M. D., & Nieto, J. M. (2006). Chemical and structural evolution of "metamorphic vermiculite" in metaclastic rocks of the Betic Cordillera, Málaga, Spain: A synthesis. *The Canadian Mineralogist*, 44(1), 249-265. <https://doi.org/10.2113/gscanmin.44.1.249>
- Salgado, S. S., de Andrade Caxito, F., Figueiredo e Silva, R. C., & Lana, C. (2019). Provenance of the Buritirama Formation reveals the Paleoproterozoic assembly of the Bacajá and Carajás blocks (Amazon Craton) and the chronocorrelation of Mn-deposits in the Transamazonian/Birimian system of northern Brazil/West Africa. *Journal South American Earth Sciences*, 96, 102364. <https://doi.org/10.1016/J.JSAMES.2019.102364>
- Santos, J. O. S. (2003). Geotectônica do Escudo das Guianas e Brasil-Central. In CPRM (Ed.), *Geologia, tectônica e recursos minerais do Brasil* (pp. 169-226). CPRM.
- Santos, J. O. S., Hartmann, L. A., Gaudette, H. E., Groves, D. I., McNaughton, N. J., & Fletcher, I. R. (2000). A new understanding of the provinces of the Amazon Craton based on integration of field mapping and U-Pb and Sm-Nd geochronology. *Gondwana Research*, 3(4), 453-488. [https://doi.org/10.1016/S1342-937X\(05\)70755-3](https://doi.org/10.1016/S1342-937X(05)70755-3)
- Sharp, Z. D. (1990). A laser-based microanalytical method for the in-situ determination of oxygen isotope ratios of silicates and oxides. *Geochimica et Cosmochimica Acta*, 54(5), 1353-1357. [https://doi.org/10.1016/0016-7037\(90\)90160-M](https://doi.org/10.1016/0016-7037(90)90160-M)
- Silva, A. R. C., Villas, R. N. N., Lafon, J. M., Craveiro, G. S., & Ferreira, V. P. (2015). Stable isotope systematics and fluid inclusion studies in the Cu-Au Visconde deposit, Carajás Mineral Province, Brazil: implications for fluid source generation. *Mineralium Deposita*, 50, 547-569. <https://doi.org/10.1007/s00126-014-0558-8>
- Simon, A. C., Knipping, J., Reich, M., Barra, F., Deditius, A. P., Bilenker, L., & Childress, T. (2018). Kiruna-type iron oxide-apatite (IOA) and iron oxide copper-gold (IOCG) deposits form by a combination of igneous and magmatic-hydrothermal processes: Evidence from the Chilean iron belt. In A. M. Arribas R. & J. L. Mauk (Eds.), *Special Publications of the Society of Economic Geologists: Metals, Minerals, and Society* (vol. 21, pp. 89-114). Society of Economic Geologists. <https://doi.org/10.5382/SP.21.06>
- Skirrow, R. G. (2022). Iron oxide copper-gold (IOCG) deposits—A review (part 1): Settings, mineralogy, ore geochemistry and classification. *Ore Geology Reviews*, 140, 104569. <https://doi.org/10.1016/j.oregeorev.2021.104569>
- Tallarico, F. H. B., Figueiredo, B. R., Groves, D. I., Kositsin, N., McNaughton, N. J., Fletcher, I. R., & Rego, J. L. (2005). Geology and SHRIMP U-Pb geochronology of the Igarapé Bahia Deposit, Carajás Copper-Gold Belt, Brazil: an Archean (2.57 Ga) example of Iron-Oxide Cu-Au-(U-REE) mineralization. *Economic Geology*, 100, 7-28. <https://doi.org/10.2113/100.1.0007>
- Tavares, F. M., Trouw, R. A. J., da Silva, C. M. G., Justo, A. P., & Oliveira, J. K. M. (2018). The multistage tectonic evolution of the northeastern Carajás Province, Amazonian Craton, Brazil: Revealing complex structural patterns. *Journal of South American Earth Sciences*, 88, 238-252. <https://doi.org/10.1016/j.jsames.2018.08.024>
- Taylor Jr., H. P. (1997). Oxygen and hydrogen isotope relationships in hydrothermal mineral deposits. In H. L. Barnes (Ed.), *Geochemistry of hydrothermal ore deposits* (pp. 229-302). Wiley. [https://doi.org/10.1007/978-1-4899-0402-7\\_6](https://doi.org/10.1007/978-1-4899-0402-7_6)
- Teixeira, N. A., Campos, L. D., Paula, R. R., Lacasse, C. M., Ganade, C. E., Monteiro, C. F., Lopes, L. B. L., & Oliveira, C. G. (2020). Carajás Mineral Province- example of metallogeny of a rift above a cratonic lithospheric keel. *Journal of South American Earth Sciences*, 108, 103091. <https://doi.org/10.1016/j.jsames.2020.103091>
- Toledo, P. I. F., Moreto, C. P. N., Monteiro, L. V. S., Melo, G. H. C., Vieira, F. M., Xavier, R. P., Carvalho, J. A., Medeiros Filho, C. A., Navarro, M. S., & Lana, C. C. (2023). Breaking up the temporal link between granitic magmatism and iron oxide-copper-gold (IOCG) deposits in the Carajás Mineral Province, NW Brazil. *Mineralium Deposita*, 59(3), 601-625. <https://doi.org/10.1007/s00126-023-01224-5>
- Toledo, P. I. F., Moreto, C. P. N., Xavier, R. P., Gao, J., de Matos, J. H. da S. N., & de Melo, G. H. C. (2019). Multistage evolution of the Neoproterozoic (ca. 2.7 Ga) Igarapé Cinzento (GT-46) iron oxide copper-gold deposit, cinzento shear zone, Carajás Province, Brazil. *Economic Geology*, 114(1), 1-34. <https://doi.org/10.5382/ECONGEO.2019.4617>
- Torres, I., Xavier, R. P., Bortholoto, D. F. A., & Monteiro, L. V. S. (2012). Hydrothermal alteration, fluid inclusions and stable isotope systematics of the Alvo 118 iron oxide-copper-gold deposit, Carajás Mineral Province (Brazil): Implications for ore genesis. *Mineralium Deposita*, 47, 299-323. <https://doi.org/10.1007/S00126-011-0373-4>
- Trunfull, E. F., Hagemann, S. G., Xavier, R. P., & Moreto, C. P. N. (2020). Critical assessment of geochronological data from the Carajás Mineral Province, Brazil: Implications for metallogeny and tectonic evolution. *Ore Geology Reviews*, 121, 103556. <https://doi.org/10.1016/J.OREGEOREV.2020.103556>
- Vale S.A. (2018). *Projeto Cururu*. Relatório final de pesquisa projeto cururu – PA. DNPM.
- Vasquez, L. V., Rosa-Costa, L. R., Silva, C. G., Ricci, P. F., Barbosa, J. O., Klein, E. L., Lopes, E. S., Macambira, E. B., Chaves, C. L., Carvalho, J. M., Oliveira, J. G., Anjos, G. C., & Silva, H. R. (2008). *Geologia e Recursos Minerais do Estado do Pará: Sistema de Informações Geográficas — SIG: texto explicativo dos mapas geológico e tectônico e de recursos minerais do estado do Pará*. CPRM. Escala 1:1.000.000.
- Wiewióra, A., & Weiss, Z. (1990). Crystallochemical classifications of phyllosilicates based on the unified system of projection of chemical composition: II. The chlorite group. *Clay Minerals*, 25(1), 83-92. <https://doi.org/10.1180/claymin.1990.025.1.09>
- Williams, P. J., Barton, M. D., Johnson, D. A., Fontboté, L., Haller, A. de, Mark, G., Oliver, N. H. S., & Marschik, R. (2005). Iron oxide copper-gold deposits: geology, space-time distribution, and possible modes of origin. In J. F. Hedenquist, J. F. H. Thompson, R. J. Goldfarb & J. P. Richards (Eds.), *One Hundredth Anniversary Volume*. Society of Economic Geologists. <https://doi.org/10.5382/AV100.13>
- Xavier, R. P., Monteiro, L. V. S., Moreto, C. P. N., Pestillo, A. L. S., Melo, G. H. C. de, Silva, M. A. D. da, Aires, B., Ribeiro, C., & Silva, F. H. F. (2012). The iron oxide copper-gold systems of the Carajás Mineral Province, Brazil. In J. W. Hedenquist & M. H. Francisco Camus (Eds.), *Geology and genesis of major copper deposits and districts of the world. A Tribute to Richard H. Sillitoe*.
- Yavuz, F., Kumral, M., Karakaya, N., Karakaya, M. T., & Yildirim, D. K. (2015). A Windows program for chlorite calculation and classification. *Computer Geosciences*, 81, 101-113. <https://doi.org/10.1016/J.CAGEO.2015.04.011>
- Zane, A., & Weiss, Z. (1998). A procedure for classifying rock-forming chlorites based on microprobe data. *Rendiconti Lincei*, 9, 51-56. <https://doi.org/10.1007/BF02904455>
- Zang, W., & Fyfe, W. S. (1995). Chloritization of the hydrothermally altered bedrock at the Igarapé Bahia gold deposit, Carajás, Brazil. *Mineralium Deposita*, 30, 30-38. <https://doi.org/10.1007/BF00208874>
- Zheng, Y. (1991). Calculation of oxygen isotope fractionation in metal oxides. *Geochimica et Cosmochimica Acta*, 55(8), 2299-2307. [https://doi.org/10.1016/0016-7037\(91\)90105-E](https://doi.org/10.1016/0016-7037(91)90105-E)